

AQUEOUS ETHANOL IGNITION AND ENGINE STUDIES, PHASE I

Final Report

KLK761

N10-11



**National Institute for Advanced Transportation
Technology**

University of Idaho

NIATT

J. Steciak, S. Beyerlein, and R. Budwig

September 2010

DISCLAIMER

The contents of this report reflect the views of the authors, who are responsible for the facts and the accuracy of the information presented herein. This document is disseminated under the sponsorship of the Department of Transportation, University Transportation Centers Program, in the interest of information exchange. The U.S. Government assumes no liability for the contents or use thereof.

1. Report No.	2. Government Accession No.	3. Recipient's Catalog No.	
4. Title and Subtitle Aqueous Ethanol Ignition and Engine Studies, Phase I		5. Report Date September 2010	
		6. Performing Organization Code KLK761	
7. Author(s) Steciak, Dr. Judi, Beyerlein, Dr. Steve, and Budwig, Dr. Ralph		8. Performing Organization Report No. N10-11	
9. Performing Organization Name and Address National Institute for Advanced Transportation Technology University of Idaho PO Box 440901; 115 Engineering Physics Building Moscow, ID 83844-0901		10. Work Unit No. (TRAIS)	
		11. Contract or Grant No. DTRT07-G-0056	
12. Sponsoring Agency Name and Address US Department of Transportation Research and Special Programs Administration 400 7th Street SW Washington, DC 20509-0001		13. Type of Report and Period Covered Final Report: August 2009 – September 2010	
		14. Sponsoring Agency Code USDOT/RSPA/DIR-1	
15. Supplementary Notes:			
16. Abstract Our objectives were to design a micro-dilution tunnel for monitoring engine emissions, measure ignition temperature and heat release from ethanol-water-air mixtures on platinum, and initiate a computational fluid dynamics model of a catalytic igniter. All three efforts progress our understanding of catalytic ignition of alternative transportation fuels. The dilution tunnel used an ejector dilutor to entrain gases and mix them with exhaust. A portable gas analyzer and particle mass monitor sensed gaseous and particulate emissions. The transportable tunnel met design criteria including a user-friendly interface and can accommodate more sophisticated gas analyzers. The surface temperature and heat generation from reactions of ethanol-water-oxygen-nitrogen mixtures on the catalyst were determined using microcalorimetry. Ignition temperatures varied from 380 K to 570 K and heat generation from 0.8 to 11.8 W/cm ² depending on the relative and absolute amounts of ethanol and oxygen. Water showed little to no effect on either the ignition temperature or the heat generation. We used a Fluent® finite volume program to model flow during the filling of a catalytic igniter. To gain confidence in modeling, a series of progressively more difficult fluid mechanics problems were solved first. This initial model is an open system with a pressure inlet. Future models will represent a closed mass system with a moving boundary.			
17. Key Words Dilution tunnel, catalytic ignition, ethanol combustion, CFD model		18. Distribution Statement Unrestricted; Document is available to the public through the National Technical Information Service; Springfield, VT.	
19. Security Classif. (of this report) Unclassified	20. Security Classif. (of this page) Unclassified	21. No. of Pages 66	22. Price ...

TABLE OF CONTENTS

Figures.....	ii
Tables.....	iii
Executive Summary	1
1. Dilution Tunnel Development	3
1.1 Description of Problem.....	3
1.2 Approach and Methodology	3
1.3 Findings; Conclusions; Recommendations.....	15
2. Catalytic Ignition of Ethanol-water mixtures on Platinum.....	17
2.1 Description of Problem.....	17
2.2 Approach and Methodology	20
2.3 Findings; Conclusions; Recommendations.....	24
3. Modelling Catalytic Plasma Torch Fluid mechanics	31
3.1 Description of Problem.....	31
3.2 Approach and Methodology	32
3.3 Findings; Conclusions; Recommendations.....	61
References.....	65

FIGURES

Figure 1.1: System diagram of dilution tunnel design..... 4

Figure 1.2: Schematic design of Labview interface. 5

Figure 1.3: Main Labview interface for data acquisition using dilution tunnel. 6

Figure 1.4: Line heater design with temperature and pressure sensor..... 8

Figure 1.5: Tunnel body with transducer and sampling lines..... 9

Figure 1.6: Side profile of sample line fittings..... 9

Figure 1.7: Control schematic for ejector dilutor. 10

Figure 1.8: NIATT dilution tunnel front view..... 12

Figure 1.9: NIATT dilution tunnel right side view. 13

Figure 1.10: NIATT dilution tunnel left side view..... 14

Figure 2.1: Experimental Setup..... 18

Figure 2.2: Ethanol and water injection cross section. 20

Figure 2.3: Process of calculating Q_{gen} , the heat generation, from reactions on the catalyst surface. .. 22

Figure 2.4: Average wire temperature vs. power for 3% fixed ethanol, 40% water. 25

Figure 2.6: Summary of ignition temperature for fixed volume dry oxygen mixtures. 27

Figure 2.5: Summary of ignition temperature for fixed volume dry ethanol mixtures. 27

Figure 2.7: Summary of surface reaction energy generation for fixed volume dry ethanol mixtures. . 28

Figure 2.8: Summary of surface reaction energy generation for dry fixed volume oxygen mixtures. . 28

Figure 2.9: Ignition temperatures for 2% fixed ethanol, dry and with 10%, 20%, 30%, and 40% water vapor. 29

Figure 2.10: Surface reaction energy generation for 2% fixed ethanol dry and with 10%, 20%, 30% and 40% water vapor. 29

Figure 3.1: Solidworks model of a catalytic plasma torch (CPT). 31

Figure 3.2: Geometry for gas dynamics models..... 34

Figure 3.3: 2D planar contour velocity map 150 kPa pressure input. 40

Figure 3.4: 2D planar contour velocity map 190 kPa pressure input. 41

Figure 3.5: 2D planar contour velocity map 500 kPa pressure input. 42

Figure 3.6: 2D axisymmetric contour velocity map 150 kPa pressure input..... 44

Figure 3.7: 2D axisymmetric contour velocity map 190 kPa pressure input..... 45

Figure 3.8: 2D planar unsteady contour velocity map at 280th time step, 0.028 sec, $\theta = 151^\circ$ 48

Figure 3.9: 2D unsteady model velocity profile..... 49

Figure 3.10: 3D CPT fluid dynamics model mesh (created in Gambit)..... 50

Figure 3.11: 3D CPT FM pressure ratio vs. crank angle plot.....	52
Figure 3.12: 3D CPT fluid dynamics model velocity vs. time step.....	52
Figure 3.13: 3D CPT velocity contour map unsteady at 280th time step, 0.028 sec, $\theta = 151^\circ$	53
Figure 3.14: 3D CPT velocity contour map unsteady at 280th time step, magnified.....	54
Figure 3.15: 3D CPT FM temperature contour map at $t = 0.0050$ s, $\theta = 27^\circ$	55
Figure 3.16: 3D CPT FM temperature contour map $t = 0.0280$ s, $\theta = 151^\circ$	56
Figure 3.17: 3D CPT FM temperature contour map $t = 0.0330$ s, $\theta = 178^\circ$	57
Figure 3.18: Summary of experimental data for air flow over the wire and results from the Fluent® and PDE models. [Leichliter, 2009]	58
Figure 3.19: 3D CPT heat transfer temperature contour map $t = 0.0334$ s, $\theta = 180^\circ$	60
Figure 3.20: Density plot of the control volume of the igniter.....	63

TABLES

Table 1.1: NIATT dilution tunnel specifications.....	15
Table 2.1: Experiment Matrix	24
Table 3.1: Isentropic Flow vs. 2D Planar SS Fluent Velocities	43
Table 3.2: Isentropic Flow vs. 2D Axisymmetric SS Fluent Velocities.....	46
Table 3.3: Summary of 3D CPT Heat Transfer Model Boundary Condition Settings.....	59
Table 3.4: Summary of Steady State Single Orifice Models.....	61

EXECUTIVE SUMMARY

Three major accomplishments were achieved during the course of this research: 1) the design and testing of a dilution tunnel for monitoring engine emissions in our Small Engine Laboratory; 2) the measurement of ignition temperature and heat release from ethanol-water-air mixtures on platinum; and 3) the initial development of a computational fluid dynamics model of a catalytic igniter. All three efforts progress our capabilities and understanding of catalytic ignition of alternative transportation fuels.

Accurate, repeatable measurement of tailpipe emissions is an important factor in the development of internal combustion engines and testing of alternative fuels. A dilution tunnel simulates the action of exhaust mixing with atmospheric gases and prevents condensation prior to gas and particulate measurements. In this work, a micro dilution tunnel was designed for the Small Engine Laboratory (SEL) and experiments were conducted to establish the controllability and accuracy of the tunnel. The tunnel design implements partial flow, Constant Volume Sampling (CVS) using an ejector dilutor. In addition to a new 5 gas Horiba MEXA 584L analyzer, a Tapered Element Oscillating Microbalance (TEOM) has been deployed for real-time measurement of particulate emissions. Data from these instruments and the flow conditioning equipment are collected and logged by a National Instruments data acquisition system.

The surface temperature and heat generation from reactions of ethanol-water-oxygen-nitrogen mixtures on a platinum wire catalyst were determined using microcalorimetry. A 127-micron diameter, 99.95% Pt coiled wire was placed crosswise in the quartz tube of a plug flow reactor. The platinum wire measured its average temperature by serving as a resistance thermometer, and enabled us to determine the amount of heat generated from surface reactions. Ignition temperatures varied from 380 to 570 K and heat generation from 0.8 to 11.8 W/cm² depending on the absolute amounts of ethanol and oxygen, the ethanol:water ratio, and the fuel-oxygen equivalence ratio. The addition of water showed little to no effect on either the ignition temperature or the heat generation on the platinum wire at the maximum 60:40 ethanol:water mole ratio (~83:17 ethanol: water liquid volume ratio) reported here. These experimental results aid in understanding the heat transfer processes of catalytic igniters used to ignite fuel-lean mixtures.

A fluid mechanics and heat transfer model of a catalytic igniter (catalytic plasma torch, or CPT) was initiated. The igniter model will help encourage discussion on design details of the igniter, especially with regard to the materials used; internal geometry; the amount and placement of platinum; and the size, location, and orientation of the orifices. We used a Fluent® finite volume model for the flow and thermal processes during the filling of a CPT. To gain confidence in modeling, a series of fluid mechanics problems were solved first. The basic 2D steady state and unsteady fluid mechanics models were calibrated by comparisons to gas dynamics compressible flow solutions. The 3D unsteady CPT model results indicate a quiescent zone at the tip of the igniter core and pockets that heat up via compression. This initial model, as formulated, is an open system with a pressure inlet. The inlet temperature is constant. Mass that is initially at the inlet temperature is added to the system. Future models will represent a closed mass system and incorporate a moving boundary to model the gas compression by the piston as it approaches the top of the cylinder.

1. DILUTION TUNNEL DEVELOPMENT

1.1 Description of Problem

Emissions from internal combustion engines are a significant concern both as potential health hazards, and as contributors to environmental issues, such as photochemical smog and climate change. Of particular interest are nitrogen oxides, carbon dioxide, carbon monoxide, hydrocarbons, and particulate matter. These pollutants can be detected by numerous methods, using either raw exhaust treated to remove water or diluting the exhaust with air to lower the dew point of the mixture.

Dilution tunnels have been shown to mimic mixing of exhaust pollutants that occurs as the exhaust exits the tailpipe of a vehicle. Additionally, the dilution process “freezes” the exhaust – preventing chemical decomposition of exhaust constituents. Most commercial solutions dilute the full exhaust flow, at a minimum of 4:1 dilution ratio. Full flow systems, however, can be very large and prohibitively expensive. Micro dilution tunnels only sample a small portion of the exhaust, which although less accurate, is significantly cheaper and smaller.

Development of a micro dilution tunnel at the University of Idaho was undertaken to expand research capabilities in engine research and emission analysis. Due to the large variety of internal combustion (IC) engine testing taking place at the University of Idaho, a dilution tunnel was chosen as the best instrument to be used in testing. Using a dilution tunnel, one can test anything from a diesel engine that generates high levels of particulate matter and NO_x, to a two-stroke engine that may release elevated levels of hydrocarbons that would saturate an ordinary gas analyzer. Additionally, the dilution tunnel does an excellent job of freezing the exhaust composition, preventing possible line contamination or continuing reactions in the hot exhaust gas. Design of the dilution tunnel was centered on meeting these research needs and goals.

1.2 Approach and Methodology

The system level design for the dilution tunnel was chosen based on several objectives: a) economy, both of size and cost; b) overall functionality; and c) ease of use.

It was decided to build a micro dilution tunnel to keep the physical envelope small, a large factor in the already crowded engine research facility. As a dilution device, an ejector dilutor was

determined to be the ideal component both due to the small physical size and the lack of moving parts. Lastly, it was decided to purchase a TEOM and portable gas analyzer as a cost effective means of providing the most functionality for sensing both gaseous and particulate emissions. These major components would be tied together using a data acquisition system running National Instruments LabVIEW[®] software. System design of the NIATT micro-dilution tunnel is summarized in Figure 1.1.

The NIATT micro dilution tunnel design dilutes a constant volume of exhaust with dilution gas. This lowers the dew point of the mixture, and enables instruments to test the mixture for pollutants without pretreatment that could modify the composition. A dilutant, which most commonly would be compressed air, is introduced as the motive flow in an ejector dilutor – drawing in engine exhaust from the suction line, and mixing it into the dilution stream; functioning as the only pumping input for the micro dilution tunnel. From the ejector dilutor, the diluted stream enters a sampling chamber, from which sample flows are drawn into various sensors.

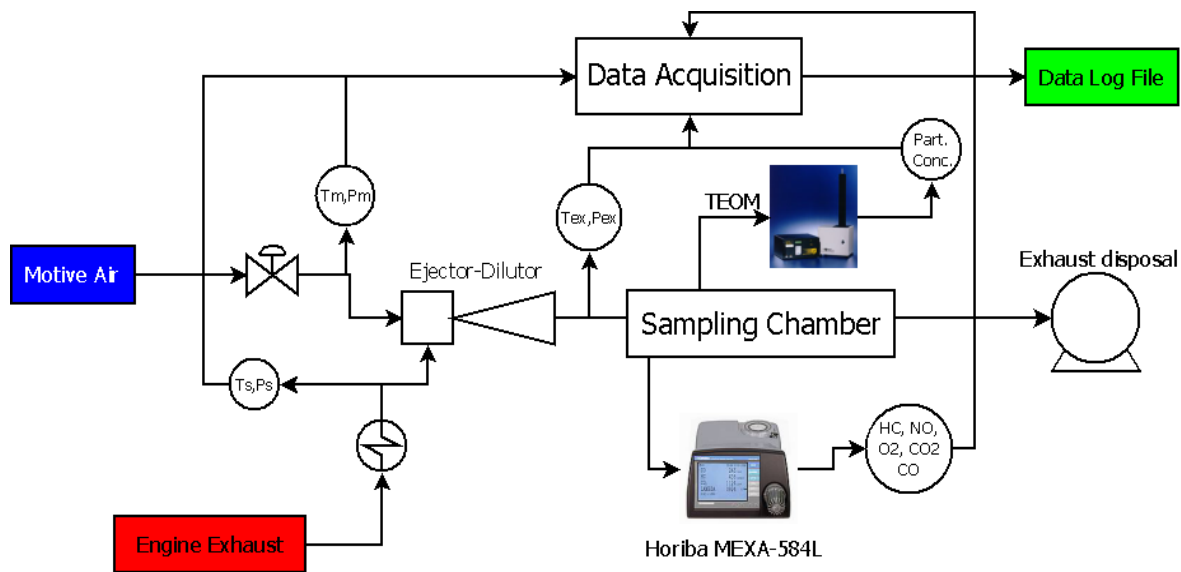


Figure 1.1: System diagram of dilution tunnel design.

Sample streams enter a gas analyzer, determining concentration of hydrocarbons, CO₂, and other pollutants. A TEOM also is connected to the tunnel, which can determine the concentration of

particulate matter in the exhaust stream. Each of these components supplies a signal to a data acquisition system that both displays the measurements and logs the data electronically. Once through the sampling chamber, the remaining dilution stream is directed out of the tunnel and into an exhaust collection system

A LabVIEW® program was created to interpret and log data from emissions instruments and collect it in a single data file. Primary design goals for this interface included: ease of use, data logging, modularity of function, and ease of access to calibration parameters. The interface was constructed in a modular fashion as shown in Figure 1.2.

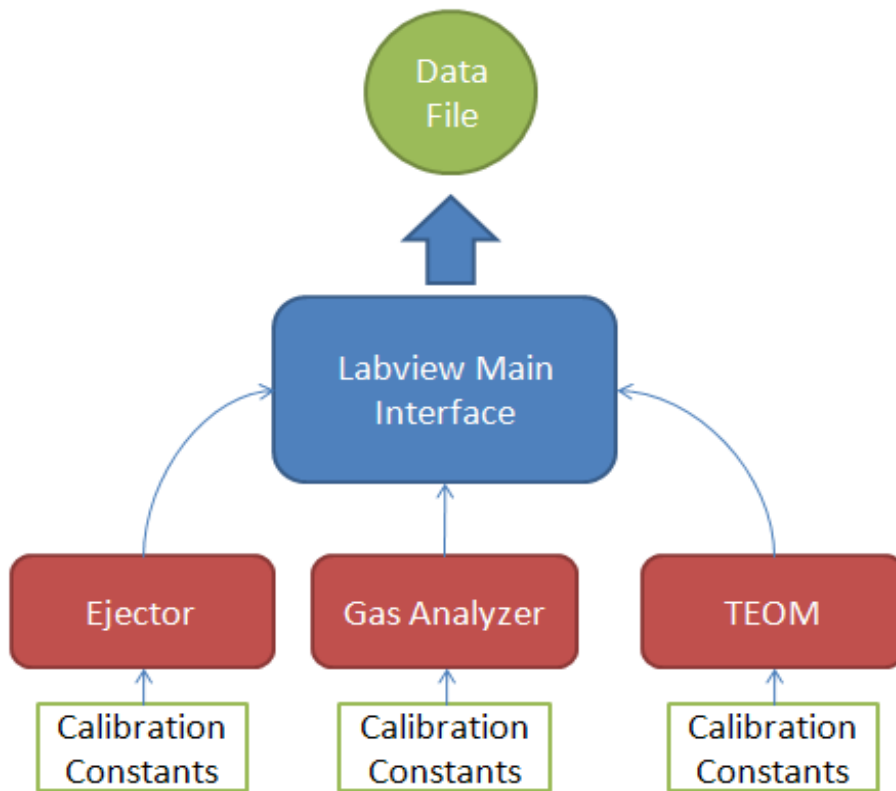


Figure 1.2: Schematic design of LabVIEW® interface.

A separate program was created for calibration and acquisition of data from each of the three major subsystems: ejector, gas analyzer, and TEOM. Each of these modules contains its own interface for calibration, and outputs for interaction with the primary interface. This design enables a user in the future to easily access calibration parameters for each of the major systems

if needed for future calibration due to instrument drift, or instrument failure. Users of the main interface do not have to view the lower modules unless necessary, as they are not displayed on the main interface. Instead, the user only has to press the start button on the LabVIEW[®] interface, specify a destination for the data file, and monitor the outputs as shown in Figure 1.3.

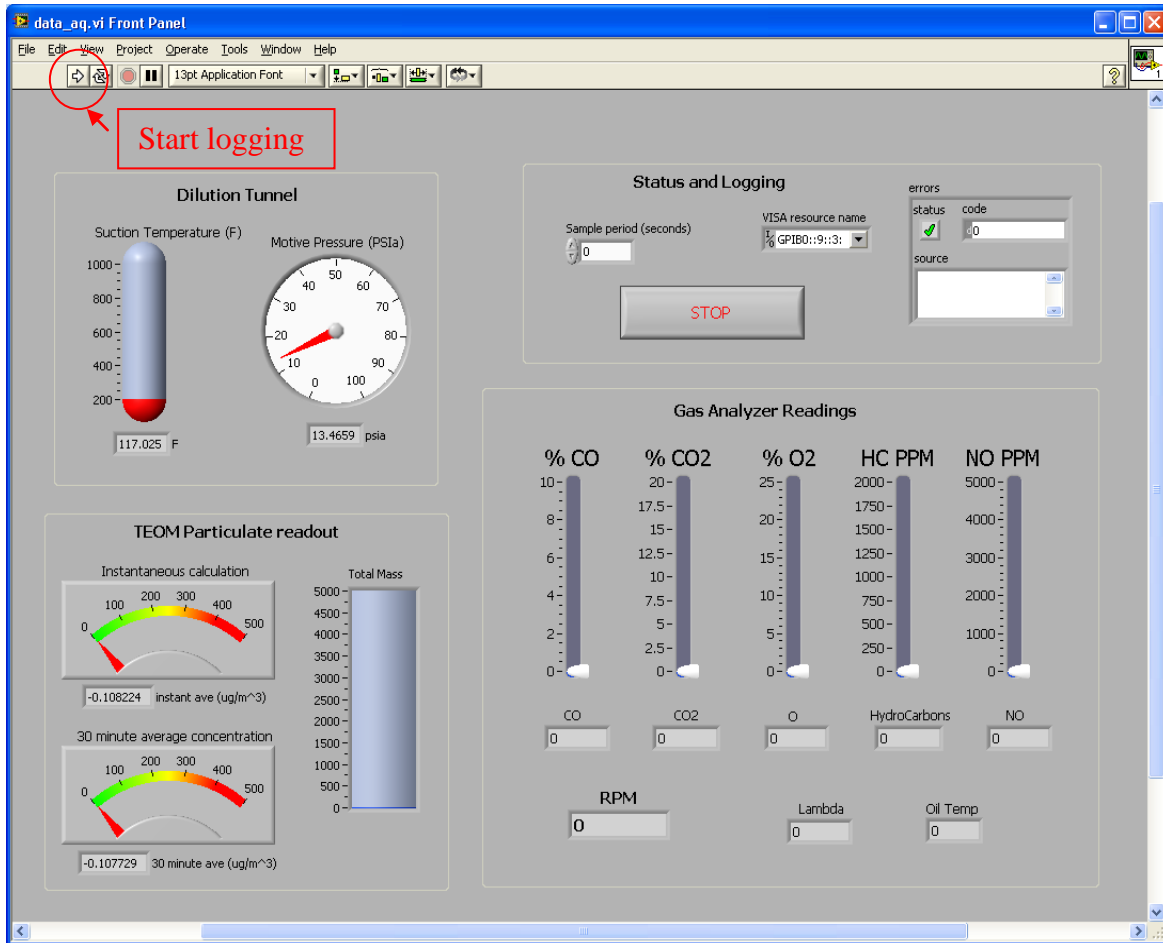


Figure 1.3: Main LabVIEW[®] interface for data acquisition using dilution tunnel.

The main interface is divided into four main sections: dilution tunnel, TEOM readings, gas analyzer readings, and status and logging. The dilution tunnel box, in the upper left of the interface, provides readings on the two major adjustment points of the dilution ratio, motive pressure, and exhaust temperature. The TEOM particulate readout, in the lower left of the

interface, displays particulate concentration both immediate, and as a 30 minute average. In addition to these readings, the total mass of particulate on the filter is displayed, as a method to determine when the filter needs to be changed. In the lower right portion of the interface is the display of emissions obtained from a Horiba 5-gas analyzer. This area of the interface displays pollutants such as CO, CO₂, NO, O₂, and HCs as well as the calculated excess air coefficient, lambda. Additionally, if the Horiba analyzer is connected to the inductive RPM sensor, or oil temp sensor, the interface will also display this data.

A method was needed to control both motive pressure and suction temperature associated with the ejector diluter. The solution was simply to install a valve upstream of the motive input to regulate motive pressure. However, increasing suction temperature proved more difficult, requiring fabrication of a line heater to increase the temperature to the desired set point.

A stainless line heater was designed to heat the incoming exhaust up to a temperature of 1000° F. This heater can be seen in Figure 1.4 below. The exhaust enters the heater at a temperature lower than desired for the dilution ratio set point. On this end of the dilution tunnel is an expansion to slow the incoming gases while they are heated. An Omegalux SST high temperature heating tape was purchased from Omega with 600 watt heating capacity. This heating tape was wrapped around a section of thin-walled stainless tubing along the body of the heater. Near the suction inlet, the heater is tapped with 1/8" pipe inputs for pressure transducer and thermocouple measurements as shown in Figure 1.4.

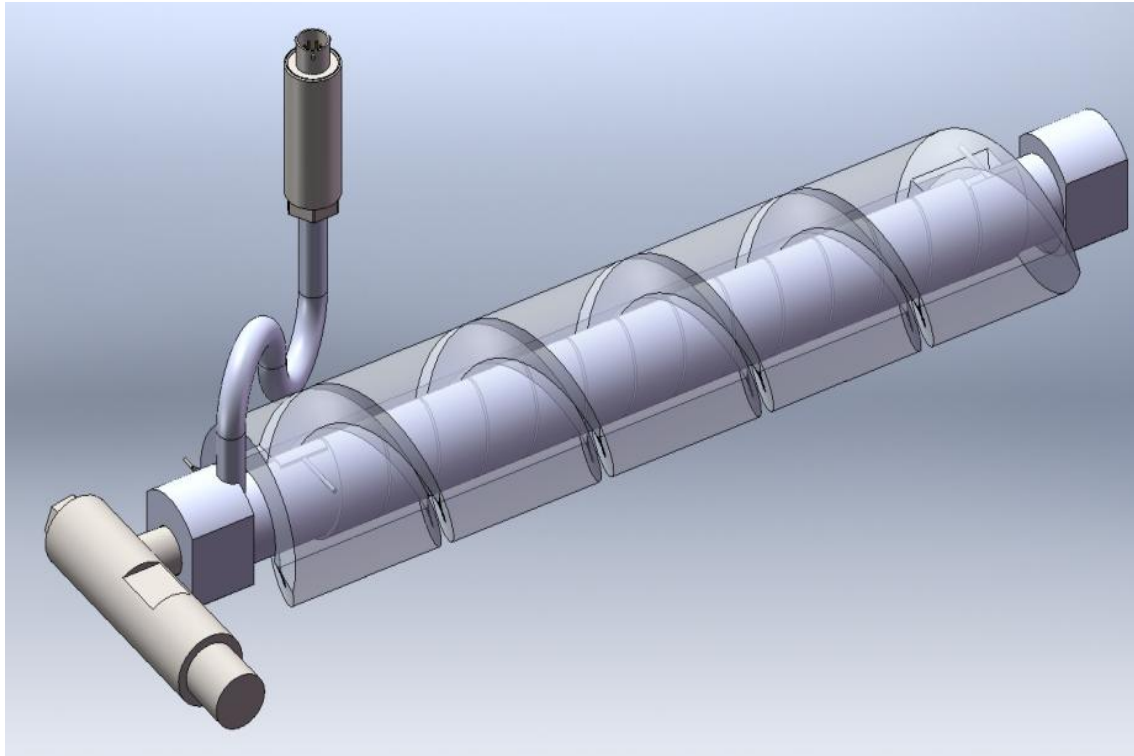


Figure 1.4: Line heater design with temperature and pressure sensor.

Due to the high temperature of the exhaust in the line heater (as high as 1200° F), it was necessary to place the pressure transducer away from the heater. This was accomplished using an “S” shaped stainless steel pressure tap, which kept the pressure transducer below its rated temperature of 450° F, while still allowing accurate pressure measurements. Additionally, due to the high temperatures, the line heater was surrounded with alumina silica ceramic fiber insulation for safety reasons.

Early testing on the ejector dilutor revealed that back pressure has a large effect on dilution ratio. As a result of this testing, care was taken to prevent back pressure downstream from the ejector dilutor. Each fitting was tapered inside with low angles to prevent pressure loss and flow separation. Fittings were added to allow the diluted flow to expand into the sampling chamber and contract to exit into an exhaust handling system. Barbed hose fittings were inserted into the sampling chamber to allow sensors to draw off diluted flow for testing as shown in Figures 1.5 and 1.6. Once the sampling chamber was completed, the dilution tunnel portion was ready for instrumentation.



Figure 1.5: Tunnel body with transducer and sampling lines.

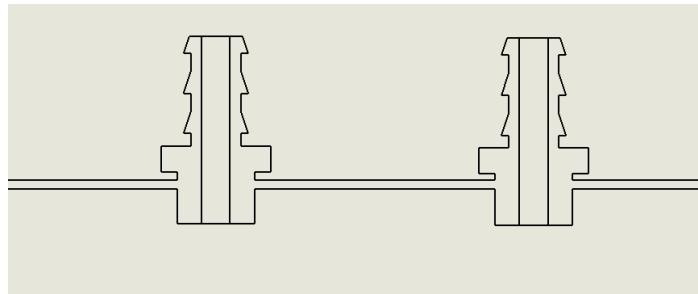


Figure 1.6: Side profile of sample line fittings.

To implement the control strategy, the dilution tunnel was instrumented with temperature sensing thermocouples and pressure transducers. Motive flow was instrumented by placing two tee fittings in line with the motive air supply. A 0-100 psia pressure transducer was connected to one of the tee fittings, while a J type thermocouple was connected to the other. As previously discussed, the suction temperature and pressure were instrumented by drilling and tapping directly into the fabricated line heater to add a thermocouple fitting and pressure tap. A 0-30

psia, high temperature, pressure transducer was attached to the top of the pressure tap. Lastly, the sampling chamber was instrumented with another 100 psia pressure transducer and J type thermocouple to provide data on the dilution stream. These sensors were connected to the VXI data acquisition unit as shown in Figure 1.7.

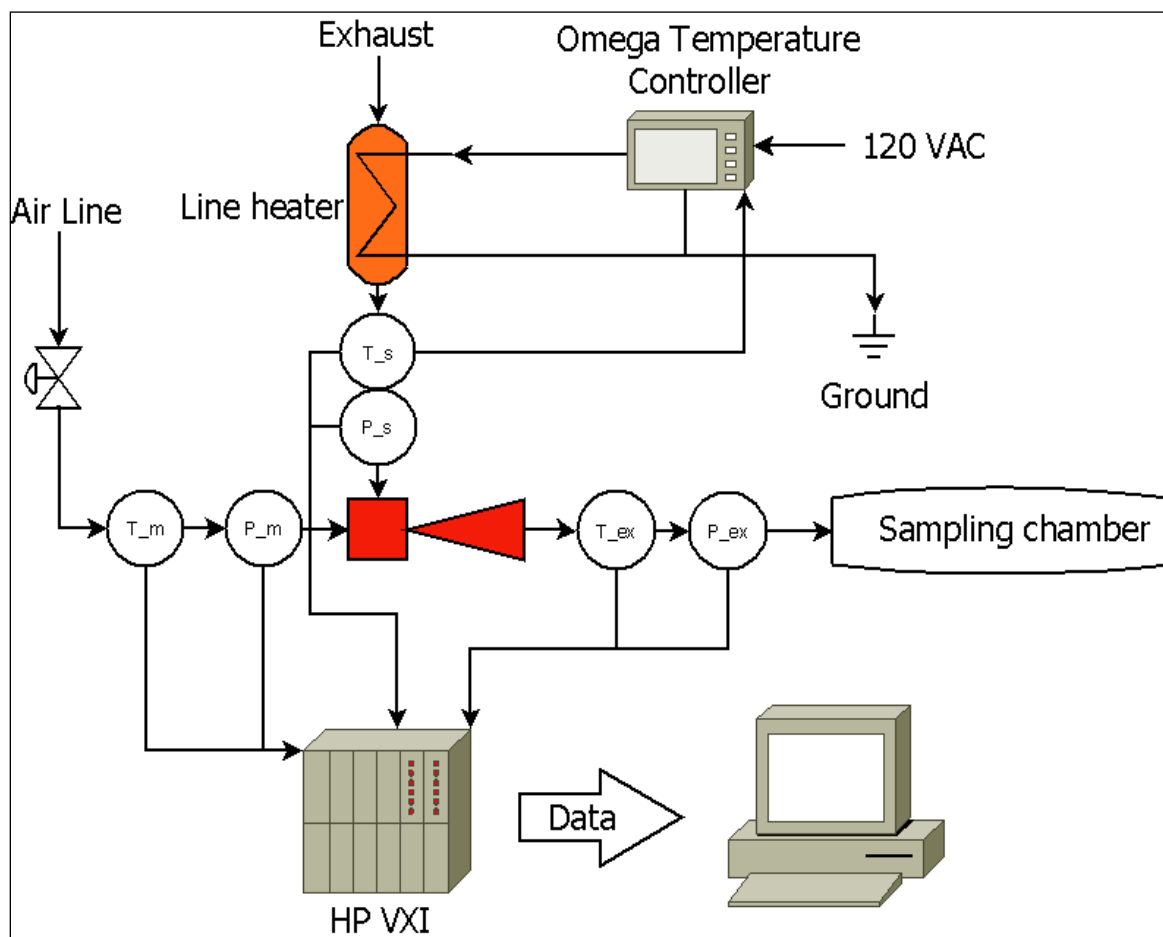


Figure 1.7: Control schematic for ejector dilutor.

To control the suction line heater, an Omega CN2110-T10 PID temperature controller was purchased and connected to the heating tape. The controller contains a 10 amp solid state relay that controls the power output to the SST heating tape, rated for 5.2 amps. This controller was connected to a switch to power the circuit. To provide temperature feedback, the controller was connected to a K type thermocouple inserted into the gas stream. This thermocouple allows the controller to monitor temperature in the suction line and adjust the power to the heating tape to maintain suction temperature.

The final stage of design and construction was to integrate all of the components together onto a single package. A single cart was designed to contain all of the working components of the dilution tunnel. An exception was made for the TEOM, which was kept separate from the tunnel cart to isolate the sensor from vibration. The final cart design, shown in Figure 1.8, implemented a recessed, shielded compartment for the suction line heater, and onboard power for line heater and computer and data acquisition. This cart concept was fabricated using steel square tube and sheet metal for construction materials. Additionally, a flexible stainless sample line was attached to the suction line to allow easy attachment to engine exhaust bungs welded into exhaust lines. The final cart setup is shown in Figure 1.8 through Figure 1.10.



Figure 1.8: NIATT dilution tunnel front view.

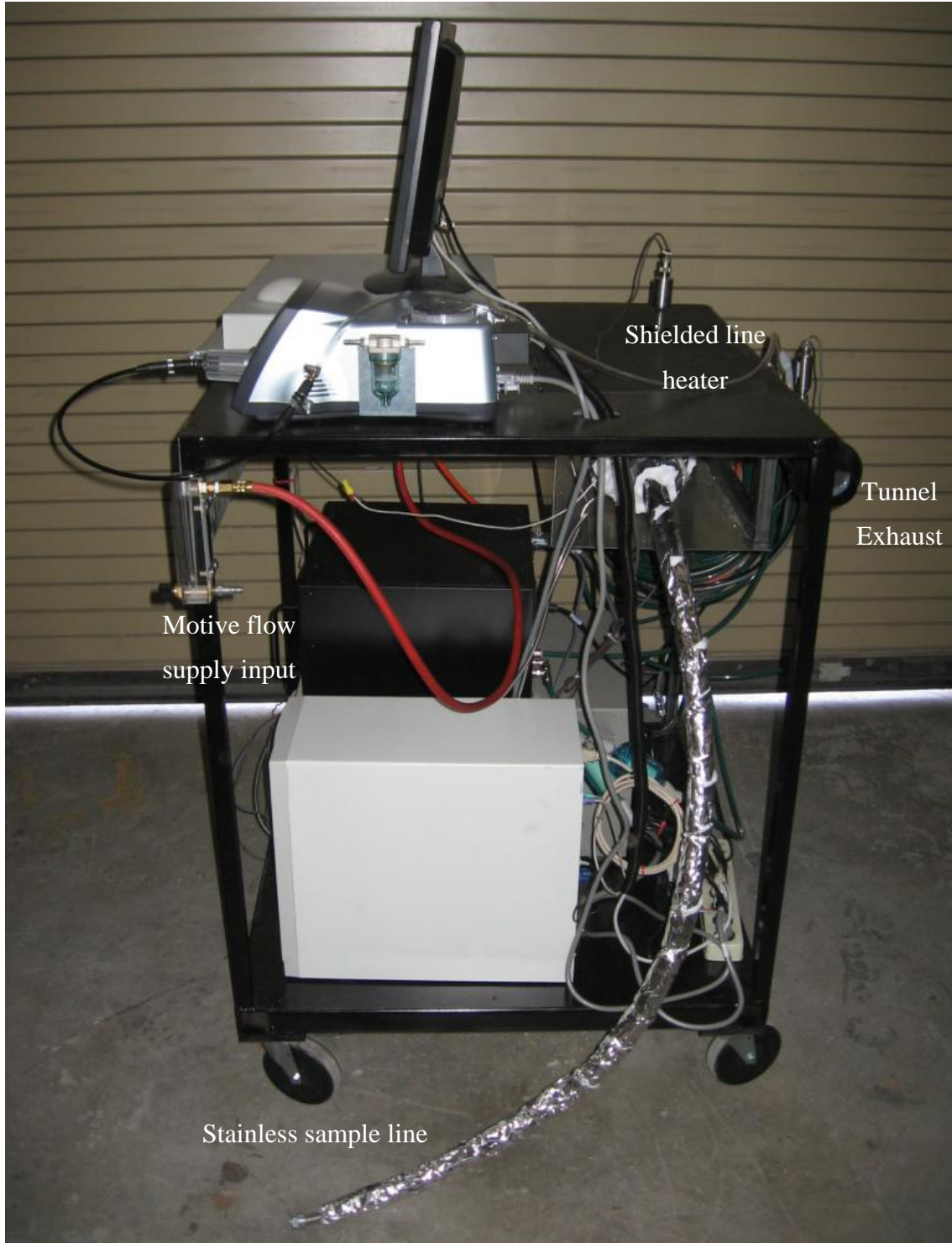


Figure 1.9: NIATT dilution tunnel right side view.



Figure 1.10: NIATT dilution tunnel left side view.

1.3 Findings; Conclusions; Recommendations

As designed and fabricated, the NIATT dilution tunnel fulfills all of the design requirements given in Table 1.1. The system is contained on a portable cart, making it ideal for the crowded environment of the Small Engine Research Facility at University of Idaho. It contains one easy-to-use interface that displays and logs all data for future use. All functions and controls necessary for operation of the dilution tunnel are located onboard the cart, meaning that the cart only needs to be connected to a power supply and air line to function. Final tunnel specifications can be found in Table 1.1.

Table 1.1: NIATT Dilution Tunnel Specifications

Sample chamber volume	2.1 Liters
Diluted exhaust flow	40-150 L/min (dilution ratio dependent)
Particulate sensor flow rate	5-13 Liters/min
Gas analyzer flow rate	4 Liters/min
Residence time	3.2 - .85 seconds (dilution ratio dependent)
Measurement Capabilities	HC, CO, CO ₂ , O ₂ , NO _x , & Particulate mass concentration
Particulate Sensor	Thermo Scientific TEOM 1400-ab
Gas Analyzer	Horiba MEXA-584L w/ NO & O ₂

Engine tests revealed two set points that should be used to set the dilution ratio at the start of testing with the dilution tunnel. Either set point can be used to good effect, although checking the dilution ratio using raw exhaust comparison is recommended before testing. Some lessons were learned in the validation of the dilution tunnel that should be heeded by future users. For particulate testing, the primary lesson learned was how sensitive the TEOM is to particulate matter and vibration. Even slight bumps or vibrations caused TEOM readings to fluctuate wildly for almost five minutes. Additionally, large quantities of particulate, such as a diesel engine produces at startup or acceleration, also create fluctuations in particulate readout that may or may not represent actual measurement of particles. Regardless of the efficacy of these measurements,

the measurements exceed the scale of the analog output from the TEOM. This scale can be changed, but would drastically affect resolution of the measured particulate matter. In short, transient particulate testing will probably not be possible without further development on the dilution tunnel and further adjustment of the TEOM itself.

Another important lesson learned in engine testing is the necessity of carefully choosing sampling locations. There are two pitfalls to avoid in choosing an area to place a sampling port in the exhaust system: exhaust air mixing and exhaust pressure. Exhaust ports should be placed at least 18 inches from the atmospheric exit of the exhaust stream to prevent induction of ambient air from the exhaust exit. Also, care must be taken to avoid pressure drops downstream of the sampling port. As engine RPM increases, this can cause back pressure in the exhaust system that could pressurize the suction line. This can be eliminated by making sure that the exhaust is sampled shortly before it exits to the atmosphere. If this is not possible, the pressure could be removed by installing a manual valve on the suction line, and creating enough pressure drop in the exhaust line to bring the suction pressure reading down to atmospheric pressure. However, this would not be desirable, due to the need to adjust this valve every time the RPM changes.

2. CATALYTIC IGNITION OF ETHANOL-WATER MIXTURES ON PLATINUM

2.1 Description of Problem

This work studied the reaction of ethanol-oxygen-water vapor mixtures, diluted with nitrogen, over a platinum wire catalyst. Our goal was to determine what effects adding water to fuel-air mixtures had on reactions on a 127- μm diameter platinum wire. The power input to the catalyst necessary to initiate surface reactions was obtained.

A plug-flow reactor was used under low Reynolds Number flow to study the interaction of ethanol-oxygen-water mixtures with the platinum catalyst. Data was collected for nonflammable fuel-oxygen mixtures. Ignition temperature, power at ignition, and surface heat generation were found for the ethanol- oxygen-nitrogen mixtures with water vapor added. Generally, the water vapor hindered the combustion process, as expected, increasing both the ignition temperature and power required for ignition, but had little effect on the heat generated due to surface reactions.

This work is part of an investigation of a CPT developed to combust very fuel lean mixtures in internal combustion engines [1-3]. Prior work obtained surface ignition temperatures and heat generation for dry and moist propane [4], and developed a model for a catalytic wire in cross flow [5]. Several studies investigated catalytic ignition of lean fuel mixtures in engines [6-11].

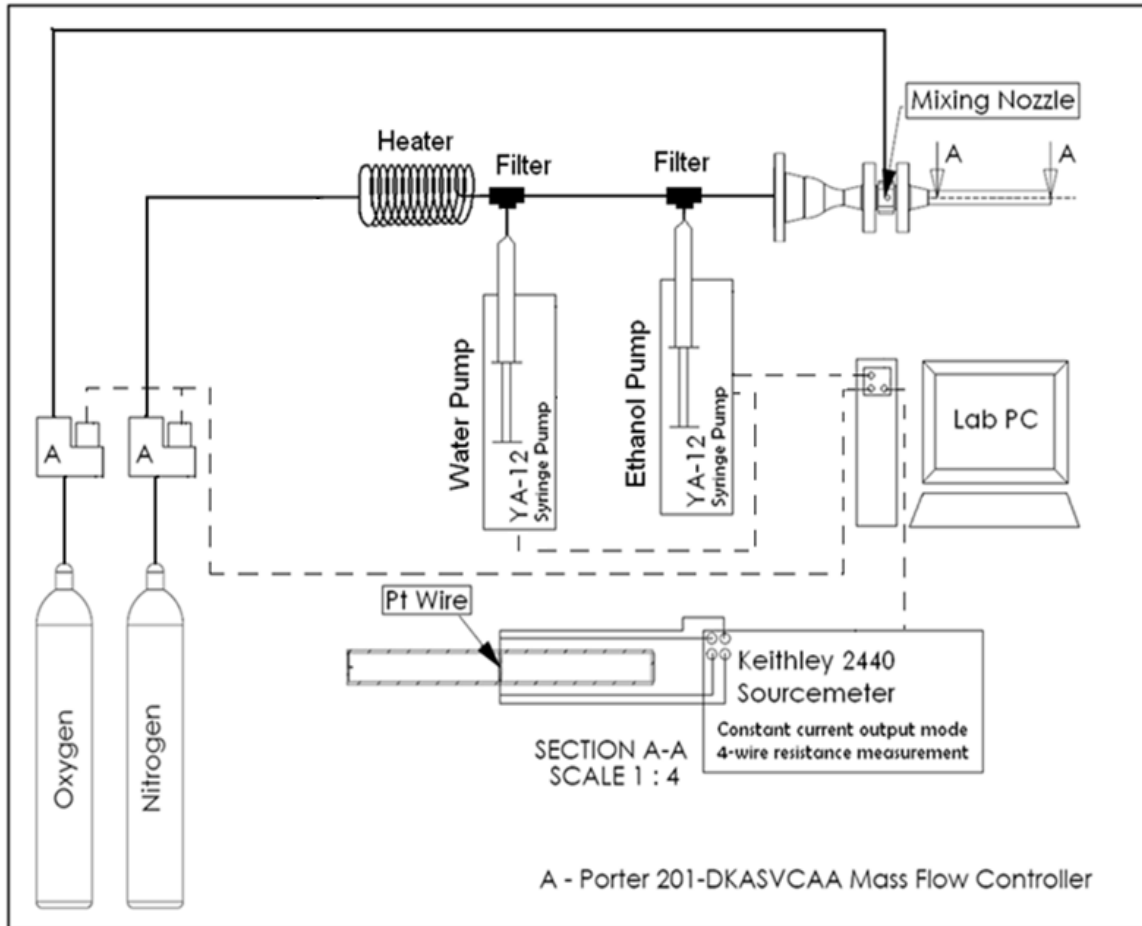


Figure 2.1: Experimental setup.

All experiments were run controlling the equipment from the lab computer using LabVIEW®. Figure 2.1 shows the experimental setup used. Nitrogen was metered through the Porter mass flow controller, which was in turn controlled with an NI-9263 analog out CompacDAQ. The flow was then confirmed by the Omega DAQ-56. Before and after liquids were injected into the nitrogen stream, the gas passed through a heating coil, constructed of $\frac{1}{8}$ inch stainless steel tubing wrapped with two Amptek electrical heating tapes. Each of these heating tapes was controlled with a variable voltage power supply, one ranging from 0-156 W and the other 0-104 W. At the injection sites, the gas stream flowed over stainless steel sintered metal wicks that Yale Apparatus syringe pumps pushed water and ethanol through, illustrated in Figure 2.2. The sintered metal filter aids heat transfer in thin film fluids [12-16] for the steady evaporation of liquid from the surface. In [4], extensive work was done in order to make sure that water was

evaporated at the same rate that it was delivered via a syringe pump. In this, work the same syringe pump and evaporator was used therefore this calibration testing was not repeated.

Three Swagelok 1/8 inch model SS-200-3 tee fittings are fitted back-to-back using 1/8 inch stainless steel tubing. A sintered filter is installed in each of the downstream fittings. A 100 micron filter was used in the water tee and a 40 micron filter was used in the ethanol tee (this micron size refers to the size of objects that will pass through the filter). Both filters were stainless steel and were acquired from Capstan in Carson, California. Each tee was machined to accommodate its sintered filter. A thermocouple was used to measure the temperature of the heated nitrogen just upstream of water injection. This measurement gave an idea of how close to the boiling point tests were being conducted to further aid in achieving steady evaporation without thermal decomposition of the fuel; for complex fuels, this temperature can be determined via thermal gravimetric analysis. The boiling point of ethanol is approximately 351 K [17-19]; we typically measured temperatures close to this in the evaporator.

Nitrogen and oxygen metered individually through Porter mass flow controllers. Each flow was again controlled then confirmed with the NI-9263 CompacDAQ and the Omega DAQ-56, respectively. The nitrogen stream was heated to evaporate ethanol and water additions at the filters. Oxygen was introduced at the mixing nozzle. The homogenous mixture exited the nozzle as a steady stream at constant velocity and traveled through the quartz tube and over the platinum coil. The coiled wire was electrically heated by a Keithley® 2440 sourcemeter. The details concerning this meter's measurements and the uncertainty of the sourcemeter were tested and discussed in [4]. In [4], the maximum average wire temperature measured 752 K, which had an uncertainty of ± 1.273 K at 9 watts. The meter used a four point measuring technique to measure the current and resistance of the platinum wire as it was electrically heated. It did so by operating in a sweep mode by slowly increasing the current. For the research presented here, the meter was again operated in sweep mode.

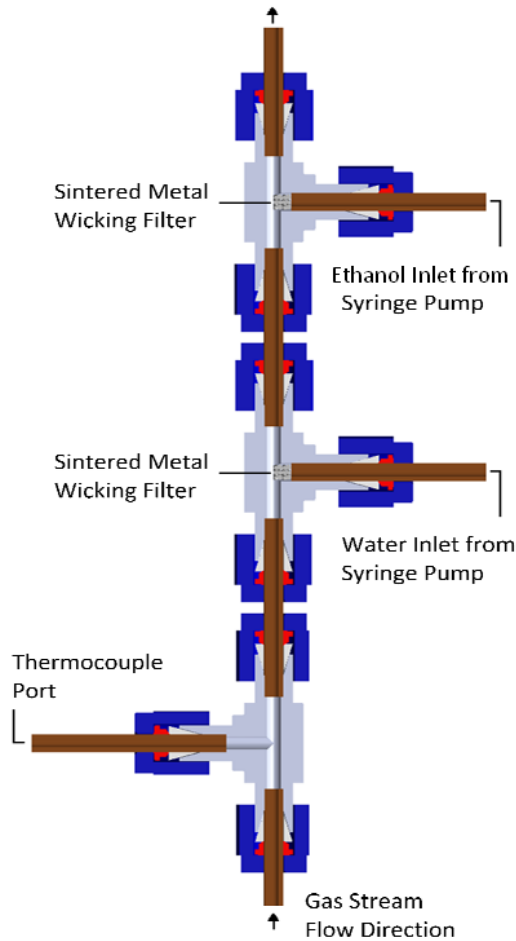


Figure 2.2: Ethanol and water injection cross section.

Letting the meter run through a sweep rather than incrementing current manually, increased the accuracy by decreasing the user error and saved time. In [4], we demonstrated that the response of the wire to changes in temperature was fast enough for the current sweep method to be accurate. A sweep from 0.6 to 1.3 amps occurred in less than one and a half minutes, slower than the ~4 second response time of the system. The maximum current reached in this work was approximately 1.5 amps.

2.2 Approach and Methodology

The platinum wire acts as a microcalorimeter, monitoring small changes in heat flow due to voltage fluctuations. By simply measuring the electrical resistance of the wire, the ignition temperature, power at ignition, and heat generation from surface reactions could be determined.

With known current and resistance values, the power input to the wire was found using Equation 2.1:

$$P = I^2 R \quad (2.1)$$

$$R = R_0 [1 + \alpha(T - T_0)] \quad (2.2)$$

The temperature of the wire was found by the linear correlation between electrical resistance and temperature [20, p 245] where R_0 is the resistance at T_0 , and α is the temperature coefficient of resistance ($\alpha=0.003927$ for platinum [21]). Using the Keithley® sourcemeter at a very low current of approximately 0.001 amps, R_0 was measured as 1.3340 Ω for $T_0 = 293$ K. These values of R_0 , T_0 and α were used as the inputs for a LabVIEW® program that calculated temperature as a function of power. Each individual test was performed a minimum of three times to ensure the results were repeatable.

Literature states that the breakdown of α for 100% pure platinum is approximately 1,100 K [22]. The Young's Modulus also changes with temperature according to the research performed by Johnson and Matthey [23]. Therefore, tests that began to reach such high temperatures were not conducted to avoid changing these properties of the platinum wire.

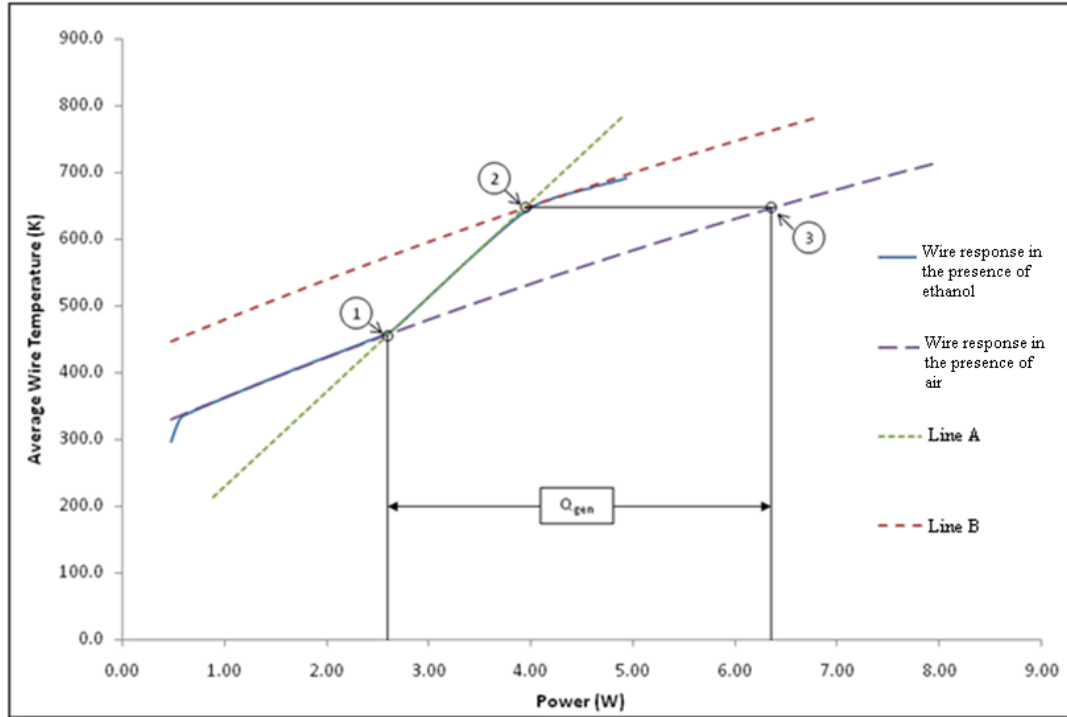


Figure 2.3: Process of calculating Q_{gen} , the heat generation, from reactions on the catalyst surface.

The uncertainty in using Equation. 2.1 lies in the resistance. However, since the Keithley® sourcemeter reads beyond the thousandths, a one-ten thousandth (0.0001) difference in resistance for R translates to an uncertainty of one-fiftieth of one degree K change in T_0 . Therefore, the uncertainty contribution of the sourcemeter in Equation 2.1 is negligible.

Resistance measurements were first taken with 5 L_{min} of air flowing over the wire. The sourcemeter was set to sweep through a range of currents, from 0.1 A to 1.7 A, while recording the wire resistance, taking 1500 readings/Amp at about 14 readings/sec. For the reactive mixtures, the peak current was set between 1.2 and 1.45 A, depending on the ethanol content, to avoid melting the wire or changing its thermal properties.

When the wire was exposed to reactive mixtures, as the power increased, the ethanol began reacting on the platinum surface, causing a jump in temperature and power and marking the ignition point. The LabVIEW® algorithm for finding this point, as well as the power generated from surface reactions, is depicted in Figure 2.3. First, LabVIEW® was programmed to calculate

a line using the steepest slope of the temperature increase with power, Line A in Figure 2.3. Line A represents the ramp-up curve between when reactions initiate and when they reach a constant rate. The intersection of this line with the air curve is considered the ignition point, Point 1. The power and temperature at this point are what will be referred to as the “ignition power” and the “ignition temperature,” or P_{ign} and T_{ign} respectively.

Figure 2.3 also illustrates the process used to calculate the heat generation from surface reactions on the platinum wire. With the response in air line programmed into LabVIEW®, tests were begun. As a reactive mixture crossed the platinum wire, the current was slowly increased using the Keithley® sourcemeter operating in sweep mode. As this occurred, LabVIEW® tracked all of the temperature data, which was recorded as the wire response in the presence of ethanol Figure 2.3. Once reactions began to occur, the wire response in the presence of ethanol line departed from the wire response in the presence of air line. This point was marked as Point 1. Point 2 represents the point at which the reactions on the platinum wire reached steady state. After this point, the reactions continued to occur and the wire’s response ran roughly parallel with the wire response in the presence of air. An algorithm connected Points 1 and 2 with a straight line that was long enough to cross the wire response in the presence of air line. The intersection of the line connecting Points 1 and 2 with the line that represented the wire response in the presence of air determined the point at which ignition occurred on the platinum wire catalyst.

If the wire in air were to be held at the temperature of Point 2, the power necessary to do so corresponds to Point 3. The energy generation, Q_{gen} , on the platinum wire is determined from Point 3, which occurs at the same temperature as Point 2. The difference between Points 1 and 3 determines the energy generation on the platinum wire surface.

Table 2.1: Experiment Matrix

FIXED C ₂ H ₅ OH	DRY	W _R = 10%	W _R = 20%	W _R = 30%	W _R = 40%
1.0%	0.1 ≤ Φ ≤	0.1 ≤ Φ ≤	0.1 ≤ Φ ≤ 0.7	0.1 ≤ Φ ≤	0.1 ≤ Φ ≤
2.0%	0.1 ≤ Φ ≤	0.1 ≤ Φ ≤	0.1 ≤ Φ ≤ 1.0	0.2 ≤ Φ ≤	0.2 ≤ Φ ≤
3.0%	0.3 ≤ Φ ≤	0.3 ≤ Φ ≤	0.3 ≤ Φ ≤ 1.0	0.3 ≤ Φ ≤	0.3 ≤ Φ ≤
FIXED O ₂					
5.0%	0.1 ≤ Φ ≤	0.1 ≤ Φ ≤	0.1 ≤ Φ ≤ 1.0	0.1 ≤ Φ ≤	0.1 ≤ Φ ≤
7.5%	0.2 ≤ Φ ≤	0.1 ≤ Φ ≤	0.2 ≤ Φ ≤ 0.9	0.2 ≤ Φ ≤	0.2 ≤ Φ ≤
10.0%	0.1 ≤ Φ ≤	0.2 ≤ Φ ≤	0.2 ≤ Φ ≤ 0.9	0.2 ≤ Φ ≤	0.2 ≤ Φ ≤
12.5%	0.1 ≤ Φ ≤	0.1 ≤ Φ ≤	0.1 ≤ Φ ≤ 0.8	0.1 ≤ Φ ≤	0.1 ≤ Φ ≤
15.0%	0.1 ≤ Φ ≤	0.2 ≤ Φ ≤	0.2 ≤ Φ ≤ 0.7	0.2 ≤ Φ ≤	0.2 ≤ Φ ≤
17.5%	0.1 ≤ Φ ≤	0.1 ≤ Φ ≤	0.1 ≤ Φ ≤ 0.6	0.1 ≤ Φ ≤	0.1 ≤ Φ ≤
20.0%	0.1 ≤ Φ ≤	0.2 ≤ Φ ≤	0.1 ≤ Φ ≤ 0.5	0.1 ≤ Φ ≤	0.1 ≤ Φ ≤

2.3 Findings; Conclusions; Recommendations

Experiments using dry and moist ethanol mixtures were conducted with a total volumetric flow rate of 5 L/min. Table 2.1 contains the experiment matrix. The 1, 2, and 3% ethanol tests were conducted under fixed molar percentages of fuel whereas the 5, 7.5, 10, 12.5, 15, 17.5 and 20% oxygen tests were conducted under fixed molar percentages of oxygen. The tests were then performed additionally with 10, 20, 30, and 40% water vapor by mole (w_r) and the balance ethanol (e.g., 90:10 ethanol:water by molar ratio). Sets of these tests were then performed with equivalence ratios of $0.1 \leq \Phi \leq 1.0$ unless otherwise noted. This approach allowed us to determine the impact of both the relative (via Φ) and absolute amounts of fuel and oxygen on the ignition temperature and heat generation as well as the impact of water.

Tests could not be conducted at all equivalence ratios for one of the following reasons: 1) the oxygen flow rate would be too low for the oxygen flow meter – valve fluttering occurred, creating unsteady oxygen flow; 2) the nitrogen flow rate would be too low to sufficiently convect ethanol through the system; 3) liquid pooling occurred in the sintered filter causing an unsteady ethanol flow rate (flooding the wick); 4) the ignition temperature would be too hot for the platinum wire to retain its original properties, specifically the temperature coefficient of resistance (α) in Equation 2.1; 5) either the ethanol or water flow rates were too low, for the pumps and the syringes used, to achieve the desired flow rates; 6) the amount of ethanol or Φ

was so low that no ignition was observed; or 7) the flow rate of water exceeded the evaporator capacity.

Data is presented based on the molar percentage of the water to the molar percentage of the ethanol. An 80:20 molar blend of ethanol and water would be about a 90:10 liquid ethanol water blend based on 0.7894 for the specific gravity of ethanol. Due to space constraints, only a small subset of data from the approximately 400 experiments will be presented and discussed here.

Typical results for wire temperature vs. power are plotted in Figure 2.4 for 3% ethanol and 40% water at $0.3 \leq \Phi \leq 1.0$, respectively. Both the solid line and short dashed line represent the temperature measured while ramping up the current sweep. The tests were conducted several times; these two curves are representative of the reproducibility of the experiments. The table shown within Figure 2.4 lists the T_{ign} (K), and Q_{gen} (W) calculated from LabVIEW® using the methods described above.

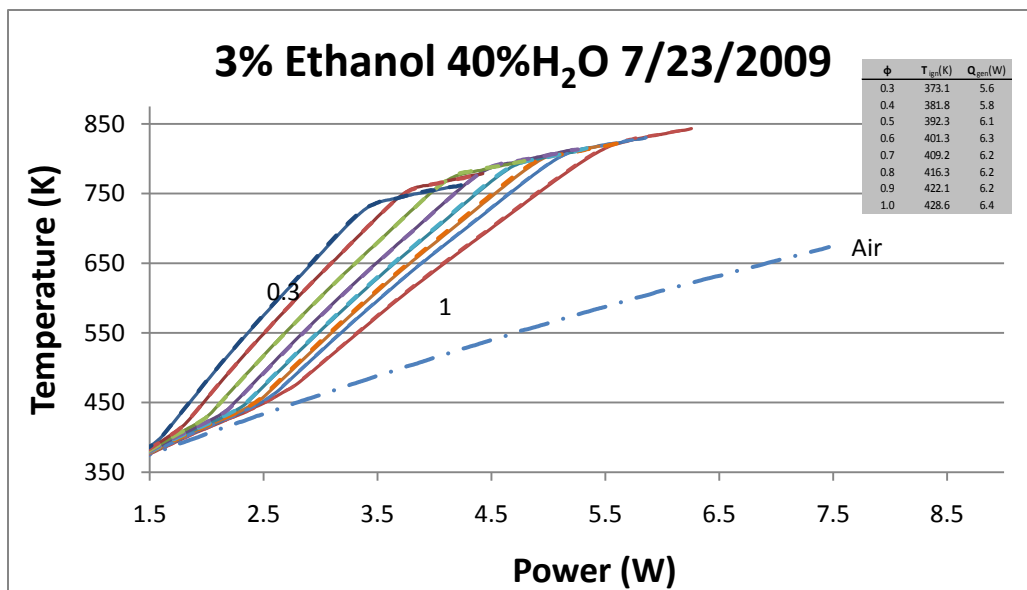


Figure 2.4: Average wire temperature vs. power for 3% fixed ethanol, 40% water.

Once all the data was collected, the ignition temperatures could be plotted as functions of the mole fractions of oxygen or ethanol, as shown in Figure 2.4 and Figure 2.5, respectively, for the dry experiments. From both Figures 2.4 and 2.5, it is evident that as the percentage of ethanol increases, or the percentage of oxygen decreases, the temperature required for ignition, and consequently the electrical power needed, increase. Therefore, mixtures with higher fuel to oxygen ratios, x_F/x_{O_2} , require more power to initiate surface reactions. This means that as the fraction of the fuel in the gas mixture is increased, the mixture is becoming less and less reactive, thus requiring a higher and higher temperature for ignition. This phenomenon may be explained by the preferential initial coverage of the surface by fuel or oxygen as discussed in [24, 25]. The way to determine as to which case a specific fuel falls under can be determined by how the ignition temperatures vary with fuel content. If the ignition temperature decreases with increasing ϕ , then the fuel-oxygen-surface would fall under initial oxygen coverage as seen by [4] for propane. However, if the ignition temperature increases with increasing equivalence ratio, then the fuel-oxygen-surface reactions would be dominated by initial fuel coverage. For the work presented here, ethanol falls under the latter, initial fuel coverage case between specific values of Φ .

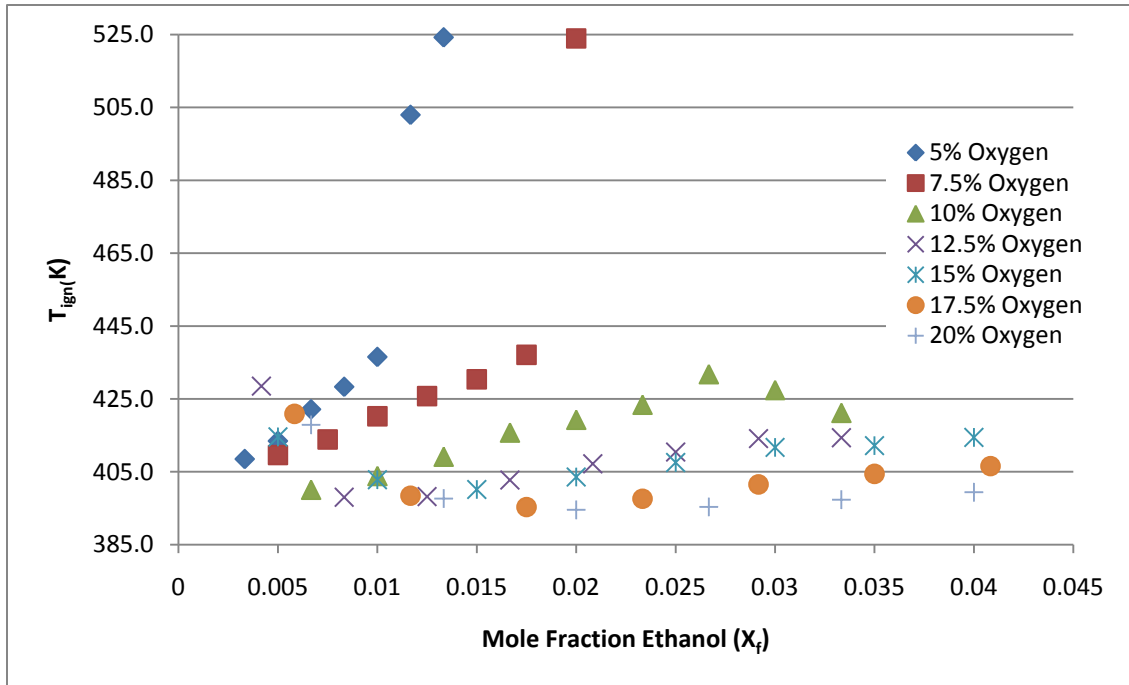


Figure 2.5: Summary of ignition temperature for fixed volume dry ethanol mixtures.

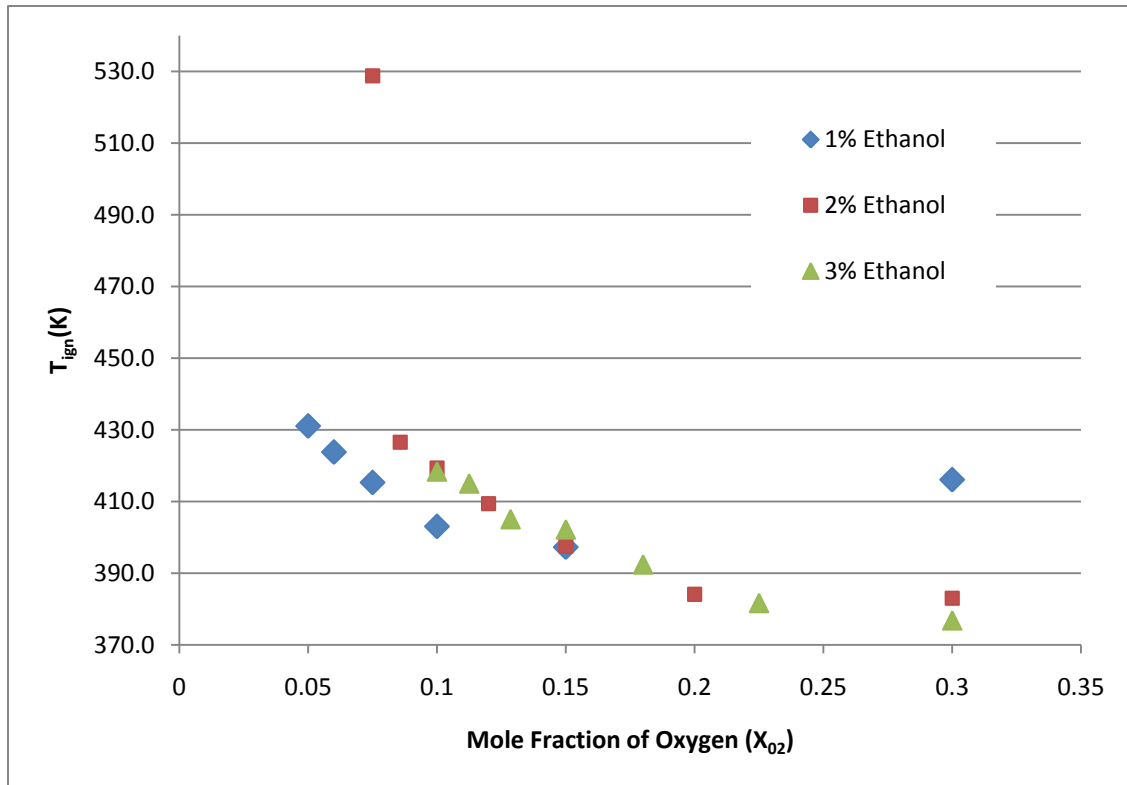


Figure 2.6: Summary of ignition temperature for fixed volume dry oxygen mixtures.

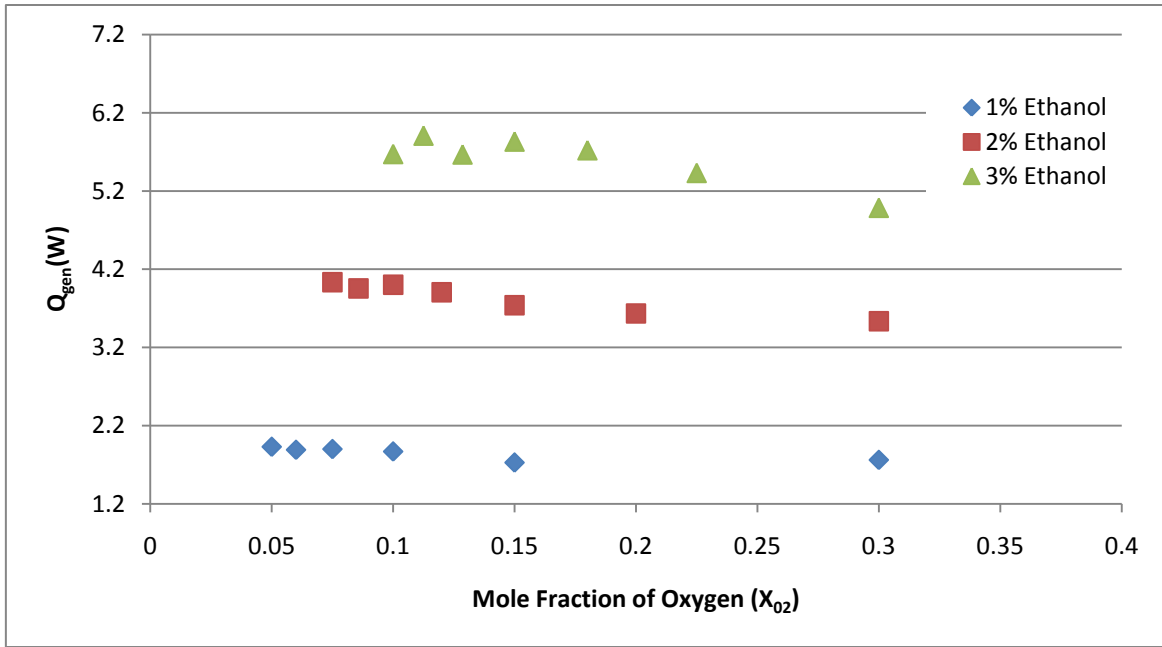


Figure 2.7: Summary of surface reaction energy generation for fixed volume dry ethanol mixtures.

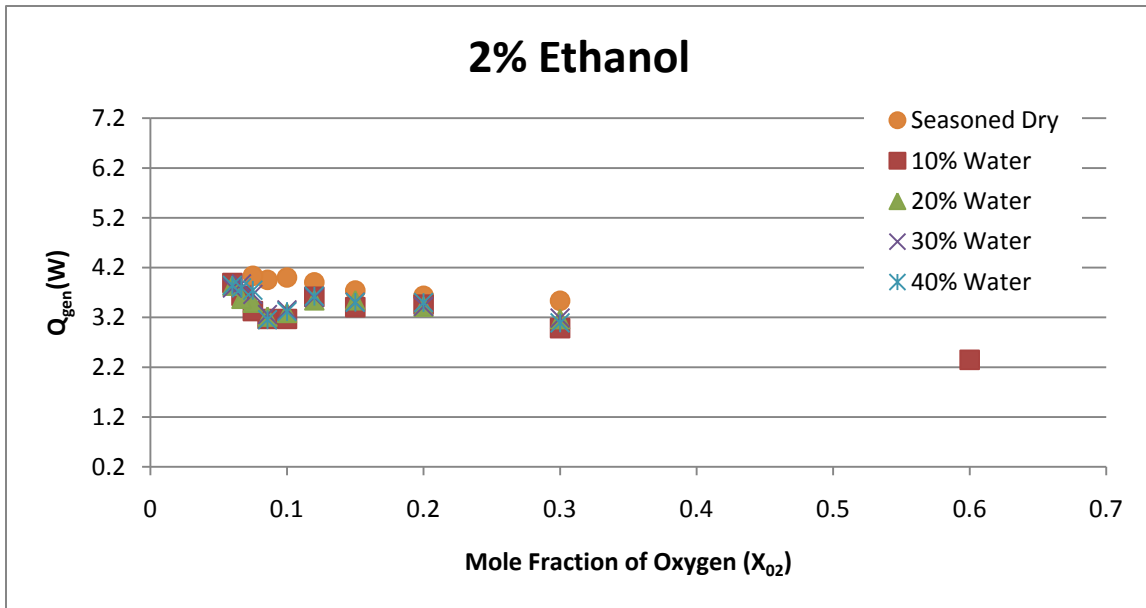


Figure 2.8: Summary of surface reaction energy generation for dry fixed volume oxygen mixtures.

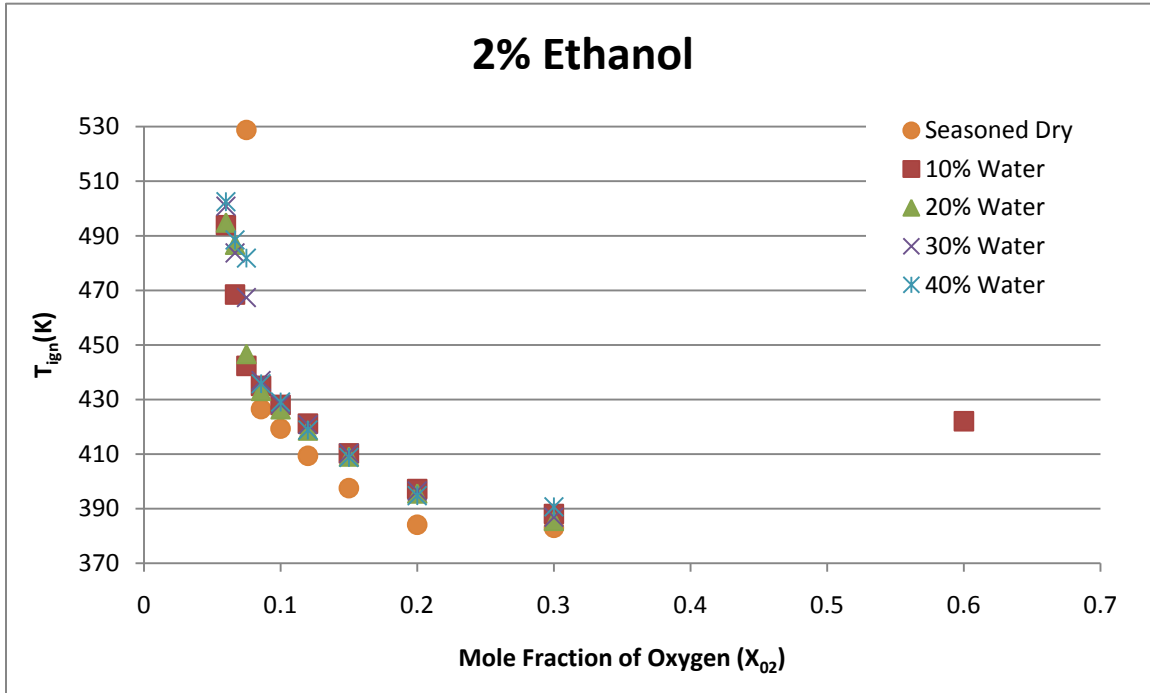


Figure 2.9: Ignition temperatures for 2% fixed ethanol, dry and with 10%, 20%, 30%, and 40% water vapor.

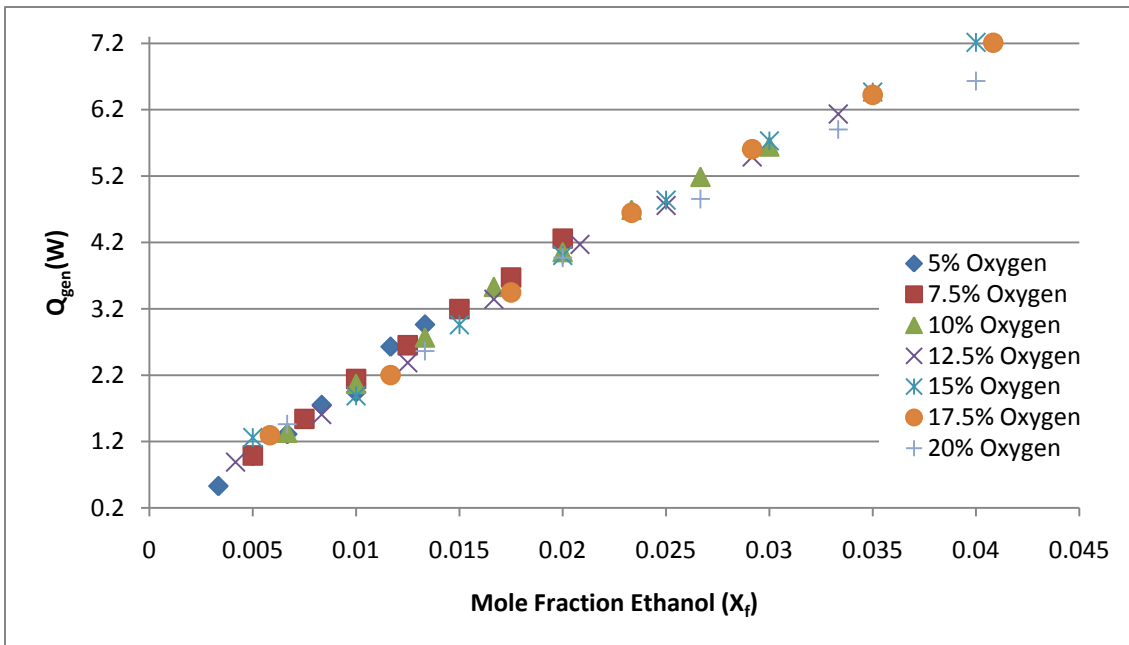


Figure 2.10: Surface reaction energy generation for 2% fixed ethanol dry and with 10%, 20%, 30% and 40% water vapor.

The results for the energy generated from surface reactions for the dry experiments are shown in Figures 2.7 and 2.8 for fixed ethanol and fixed oxygen, respectively. The trend is more evident from the fixed oxygen data, but both plots show more energy generated from the surface reactions with higher ethanol and lower oxygen content.

One of the goals of this study was to research the effects of adding water vapor to the reacting mixtures. Figure 2.9 compares the ignition temperatures of dry mixtures with those for increasing amounts of water vapor added for fixed ethanol content (2%). The temperature required for ignition appears to increase slightly with increasing water content at oxygen levels above 5%. Energy generation appeared to decrease slightly as more water was added to the system (Figure 2.10). Both these trends are not marked at the water content reported here.

Ethanol exhibits initial fuel coverage behavior on platinum in contrast with initial oxygen coverage fuels such as propane. Hence, more catalyst heating is required to initiate surface reactions with increasing equivalence ratio in fuel lean mixtures; ignition temperatures increase as the equivalence ratio increases. Once ignition occurs, the amount of energy released increases with increasing equivalence ratio.

In general, the addition of water increased the electrical power and temperature required for ignition, and reduced the energy generation from the reaction. However, the changes were not marked. This result implies that the surface reactions are not significantly affected by the amount of water in the mixtures reported here.

Future plans include expanding the capacity of the evaporator. This will allow higher flow rates of liquid fuels and water, and the testing of heavy fuels that will be more difficult to vaporize without decomposition.

3. MODELLING CATALYTIC PLASMA TORCH FLUID MECHANICS

3.1 Description of Problem

A 3D unsteady catalytic igniter (catalytic plasma torch or CPT; Figure 3.1) model including fluid mechanics, heat transfer, surface kinetics, and gas-phase combustion would allow us to explore the initial ignition of fuel-air mixtures adjacent to the Pt core and changes in CPT geometry, materials, and fuel-air properties that affect ignition timing. This project initiated the development of a thermal-fluid model of a CPT. To set the stage for fluids modeling of the catalytic igniter, a methodology for verifying computational fluid dynamic (CFD) models that are too complicated for detailed data or analytical analysis was developed and applied.

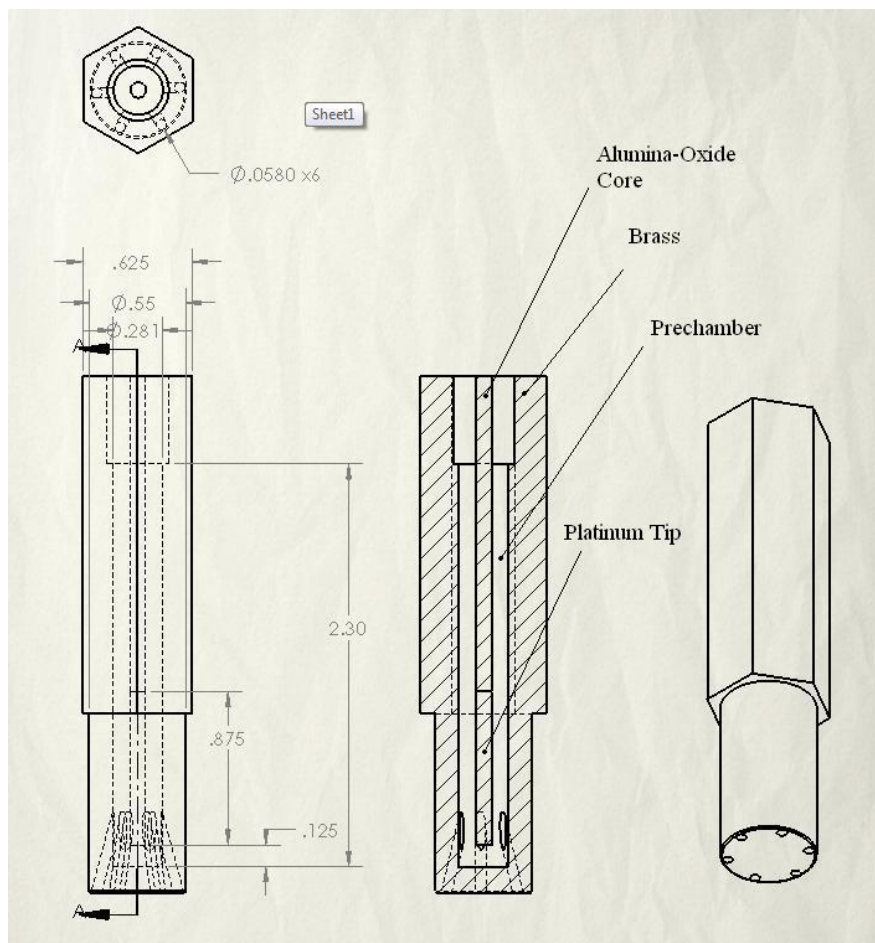


Figure 3.1: Solidworks model of a catalytic plasma torch (CPT).

3.2 Approach and Methodology

Computational fluid dynamics (CFD) provides a method to research and investigate fluid flow and heat transfer within the body of the catalytic igniter. Numerical simulations of the catalytic igniter allow the continuity, momentum, and energy equations to be solved at the nodes within a two- or three-dimensional grid imposed on the flow field.

The governing equations are listed below in the following order: conservation of mass, conservation of momentum (Navier-Stokes), and the conservation of energy equation. Each is solved within a computational mesh; whether that is nodal-based or cell-based is chosen by the user. The research, study, and advancement of these equations are integral to computational fluid dynamics.

Conservation of mass is defined by (3.1):

$$\vec{\nabla} \cdot (\rho \vec{v}) + \frac{\partial \rho}{\partial t} = 0 \quad (3.1)$$

Where ρ is mass density, v is velocity and t is time. This condition must be satisfied at every point in the fluid.

The conservation of momentum, or Navier-Stokes, equation represents the physical balance between the change of momentum and stresses in the flow field. The left side of the equation represents the inertial forces comprised of the unsteady acceleration and the convective acceleration. The first term on the right side of the equation is the body force, the second is the gradient of pressure p (pressure force) and the third represents the viscous forces (μ is fluid viscosity).

$$\rho \frac{D\vec{v}}{Dt} = \rho g - \vec{\nabla} p + \mu \vec{\nabla}^2 \vec{v} \quad (3.2)$$

Conservation of energy is represented by (3.3). This is the energy balance between the rate of change of internal energy on the left hand side and diffusion of energy, change in potential energy and heat generation on the right hand side.

$$\rho \frac{DU}{Dt} = \vec{\nabla} \cdot (k \vec{\nabla} T) + \frac{Dp}{Dt} + \Phi \quad (3.3)$$

Where U is the internal energy storage, k is the thermal conductivity of the fluid and T is the temperature field.

The tool that is being used in this research is Fluent, a computational fluid dynamics program that was first developed in 1988.

Each initial calibration model consists of a single orifice that is either 2D planar or 2D axisymmetric. The diameter of the orifice for each model is the diameter of one orifice of the actual igniter. This was done to simplify the model because we wanted to understand and be able to account for possible high velocity through the orifice. The diameter or width of each model is also the diameter of the catalytic igniter's pre-chamber.

The diameter of the upstream chamber was chosen carefully to avoid entrance effects or computational inefficiencies.

The duration of each time step was chosen by considering the operation of the Cooperative Fuels Research (CFR) engine in the Small Engine Laboratory. The engine's idling speed ranges between 500 and 900 RPMs [Anderson, 2009]. The engine speed chosen was 900 RPMs. With this speed the amount of time it takes to complete one revolution of the crankshaft is 0.0668 seconds or 668 time steps at increments of 0.0001 seconds. This time step was used for all of the unsteady models.

The pressure inlet is located at the bottom edge/face of Figure 3.2. With the steady state models, the top edge/face was set to a pressure outlet instead of wall to compare and contrast the velocities computed with velocities calculated from isentropic flow tables.

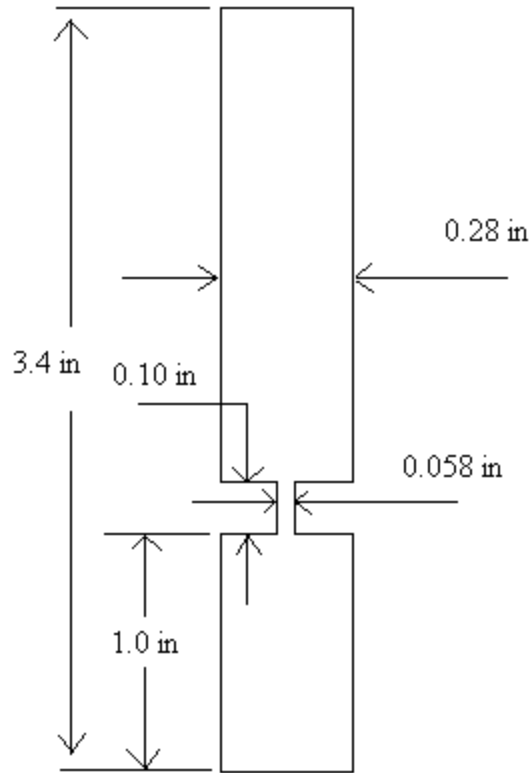


Figure 3.2: Geometry for gas dynamics models.

One factor in CFD that is important to understand is convergence. The residual for a solution variable – continuity, velocity components, energy, and turbulence variables – is the change in the solution variable from one iteration to the next. Convergence is achieved when the residuals are less than or equal to the user’s criteria.

Fluent allows the user to provide values for the solution variables in an attempt to accelerate convergence. If a solution has converged but these ‘first guess’ values do not reflect reality, then the solution should be examined for plausibility. When a solution does not converge, does not diverge, and the residuals “flat line” the solution should always be looked at for reasonability. If velocities are misjudged, divergence can take place in the iterative solution process or even converge with a nonsense solution.

The solution accuracy can be affected by selecting a first order or second order (with respect to the grid spacing in the solution domain and/or the time step) discretization scheme for the different governing equations.

Solver

The solver is the heart of the computational fluid dynamics software. There are two choices: pressure-based (segregated) solver and density-based (coupled) solver. The density-based solver solves all of the equations (conservation of mass, momentum, and energy) simultaneously whereas the pressure-based (segregated) solves the equations separately. It is recommended to use the density-based solver when the pressure and velocity are strongly coupled as they are in flows at very high pressures and velocities. The density-based solver was used in the initial single orifice models where the velocities approached the speed of sound through the orifice. The pressure-based solver was used for the final 3D CPT model.

Turbulence Models

The turbulent governing equations have a closure problem within the viscous terms. Numerous equations have been derived in order to solve this closure problem. While some of the turbulence models have been created to be robust in multiple applications, such as the standard k- ϵ model, others have been created with specific applications in mind, for example, for situations with strong adverse pressure gradients along an airfoil that are addressed with the shear-stress transport (SST) k- ω model. The wide range of turbulence models poses a challenge for the user: which is the best choice for the specific application of interest?

In the preliminary, or gas dynamics, models, the Spalart-Allmaras turbulence model was used for solving high speed enclosed flows. This turbulence model had worked well for CFD research on a micro propulsion rocket nozzle in similar high speed flows [Plumlee, 2007]. When solving the 3D single orifice model with the Spalart-Allmaras choice, divergence occurred with the molecular kinematic viscosity (ν_t) and also with two of the velocity components. This led to changing the turbulence model to the standard turbulent k- ϵ model and convergence was reached with the new setting. The standard turbulent k- ϵ model has proven to be robust and suitable for use with the 3D CPT models.

Boundary Conditions

Boundary conditions are necessary for the Fluent software to begin solving the governing equations. Boundary conditions for walls, inlet and outlets of the steady state models and the inlets of the unsteady models are set as discussed below.

Pre-chamber and Upstream Walls

There is no mass transfer across the physical walls.

The setting of the no slip condition (zero velocity at the wall) was applied to all of the walls in every model.

An adiabatic wall boundary condition was chosen because of the time frame of an initial cold start-up. The penetration distance of a thermal wave can be estimated by taking the square root of the product of material thermal diffusivity and time increment being analyzed (3.4):

$$d \cong \sqrt{\alpha t} = \sqrt{8.17E(-10) \frac{m^2}{s} \cdot 0.0334 \text{ sec}} = 0.005 \text{ mm} \quad (3.4)$$

where d is the thermal wave penetration depth into the wall, α is the thermal diffusivity of brass, and t is the time of interest. The resultant characteristic penetration depth for brass was 0.005 mm or 5 μm , hence negligible heat loss to walls is expected and the adiabatic wall assumption is reasonable.

Steady State Inlet and Outlet

The mass entering is the amount of mass leaving. Three pressure inputs were chosen because we wanted a pressure ratio at the choked condition as well as one below and one above. Hence, we would cover sonic, supersonic, and subsonic flow. Three different pressure inputs are used in the first of the steady state models - the 2D planar will look at a 150 kPa, 190 kPa, and 500 kPa case. In the 2D axisymmetric steady state model, the 500 kPa case was dropped. The pressure outlet was always set to one atmosphere.

Unsteady Inlet

The pressure function is derived from the kinematic equation of piston motion combined with the polytropic equation from thermodynamics. This will yield a pressure as a function of crank angle, geometric engine lengths, ratio of specific heats, and the pressure of the cylinder at bottom dead center (BDC). The pressure function is shown below.

$$P_1(t) = P_{\text{BDC}} \left(\frac{(L + 2r)}{L + r + l - (r \cos(\omega t) + \sqrt{l^2 - r^2 \sin^2(\omega t)})} \right)^k \quad (3.5)$$

$P(t)$ is the pressure as a function of time, P_{BDC} is the pressure at bottom dead center (BDC), L is the clearance length between the piston and the head at top dead center (TDC), r is the crank arm radius, l is the connecting rod length, ω is the engine speed in radians/s, and t is time.

Flow reversal is allowed to occur over this boundary condition because flow will be kept at a certain pressure along the boundary.

Alumina Oxide Core

In the fluid mechanics CPT model, the core's walls are modeled as adiabatic.

In the heat transfer CPT model, the walls of the core tip and their corresponding shadow wall are coupled thermally. This is done so that heat transfer will be calculated correctly between the shadow wall and corresponding physical wall. There is also a cell zone energy source term applied to the core tip. Convection heat transfer is modeled as the boundary condition between the fluid and the heated tip.

2D Single Orifice Steady State (SS)

The formulation of each model in the series progressed so that the results from a prior model would yield insights regarding the approach needed for the next computational model. The first model produced was a single orifice steady state model in various dimensions.

Analytical Model Formulation, 2D SS Single Orifice

The governing equations for the 2D single orifice steady-state model formulation are those for the isentropic compressible flow of air through a truncated orifice or nozzle.

$$c = \sqrt{kRT} \quad (3.6)$$

$$\frac{p_*}{p_t} = \left(\frac{2}{k+1} \right)^{k/(k-1)} \quad (3.7)$$

$$M_e = \sqrt{\frac{2}{k-1} \left[\left(\frac{p_t}{p_b} \right)^{k-1/k} - 1 \right]} \quad (3.8)$$

For each of these gas dynamics equations, the variables are defined as: c is the speed of sound through a fluid; k is the ratio of the specific heats; p_* is the pressure at which the orifice flow is choked (the Mach number is one through the orifice and the maximum mass flow rate has been achieved); p_t is the stagnation pressure; and M_e is the Mach number through the orifice.

The calculated speed of sound through the orifice is 347 m/s. The pressure at which the orifice flow will be choked is 190 kPa. The resultant Mach number for a 150 kPa pressure input is about 0.7701 or a velocity of 270 m/s. With 190 kPa, the Mach number is 0.998 or 346 m/s. With a different pressure input of 500 kPa, the Mach number is 1.7 or a velocity of 590 m/s.

Boundary Conditions

The boundary conditions consist of constant mass at inlet and outlet, three different pressure inlet values, an atmospheric pressure outlet, no slip condition at the walls, all walls are adiabatic, and an assumed temperature of 300 K. The input pressures will yield an orifice velocity to be compared with the gas dynamics solution.

Fluent Results

For the 150 kPa pressure input case shown in Figure 3.3, the orifice velocity is 284 m/s. The exit flow exhibits a Coandă effect, i.e., the wall prevents fluid from being entrained into the jet which causes the jet to lean into the wall. The upstream entrance effects of the fluid into the orifice are not affected by the distance between the orifice and the wall. So the choice of the width of the main chamber works well.

For the 190 kPa pressure input show in Figure 3.4, the velocity through the orifice is at 366 m/s. The flow is choked at this pressure ratio.

The 500 kPa pressure input solution in Figure 3.5 has an orifice velocity of 627 m/s. The presence of the velocity increasing after the orifice signifies that the nozzle is choked. This boundary condition was chosen because we did not know initially what velocity to expect. This was the extreme. After unsteady cases were explored, we found there was no need to study flow past sonic conditions.

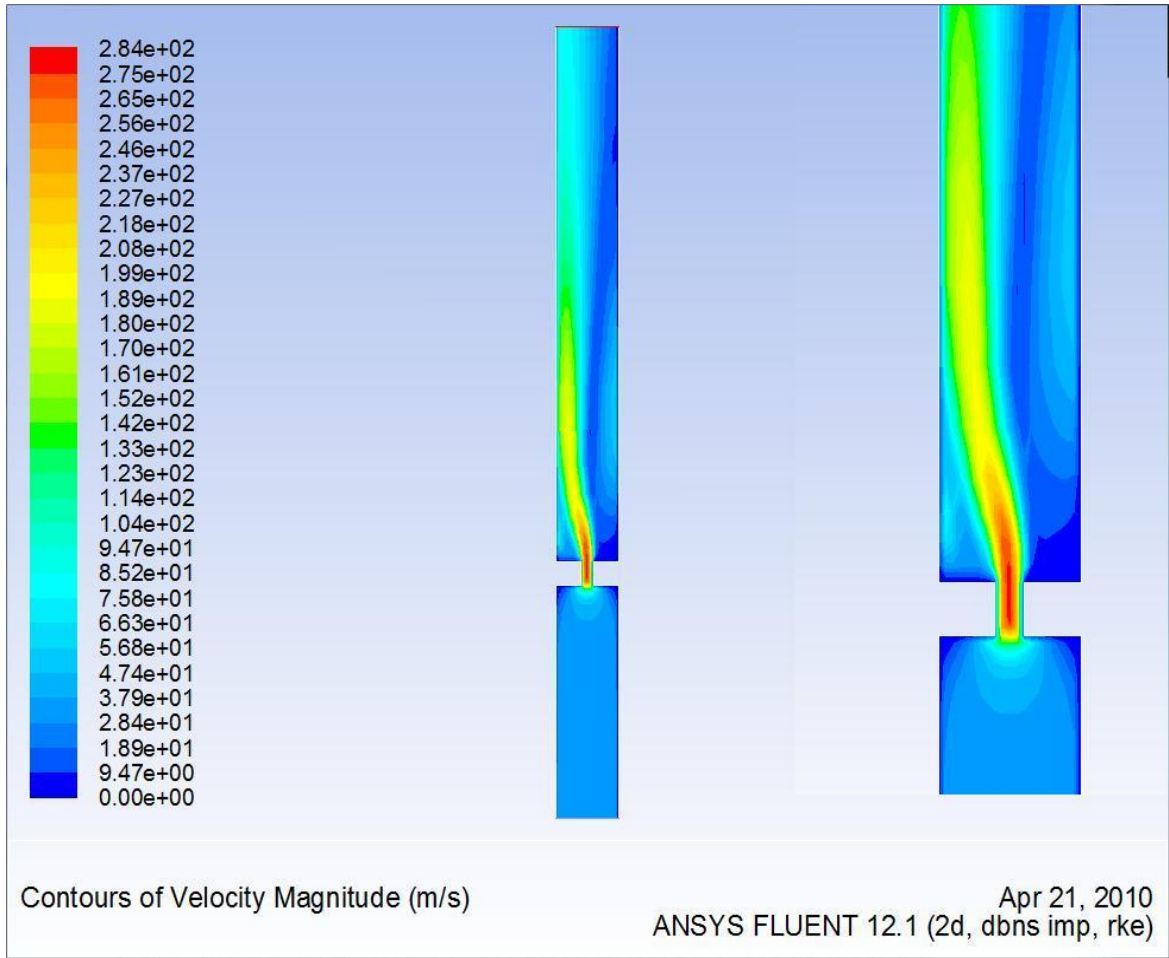


Figure 3.3: 2D planar contour velocity map 150 kPa pressure input.

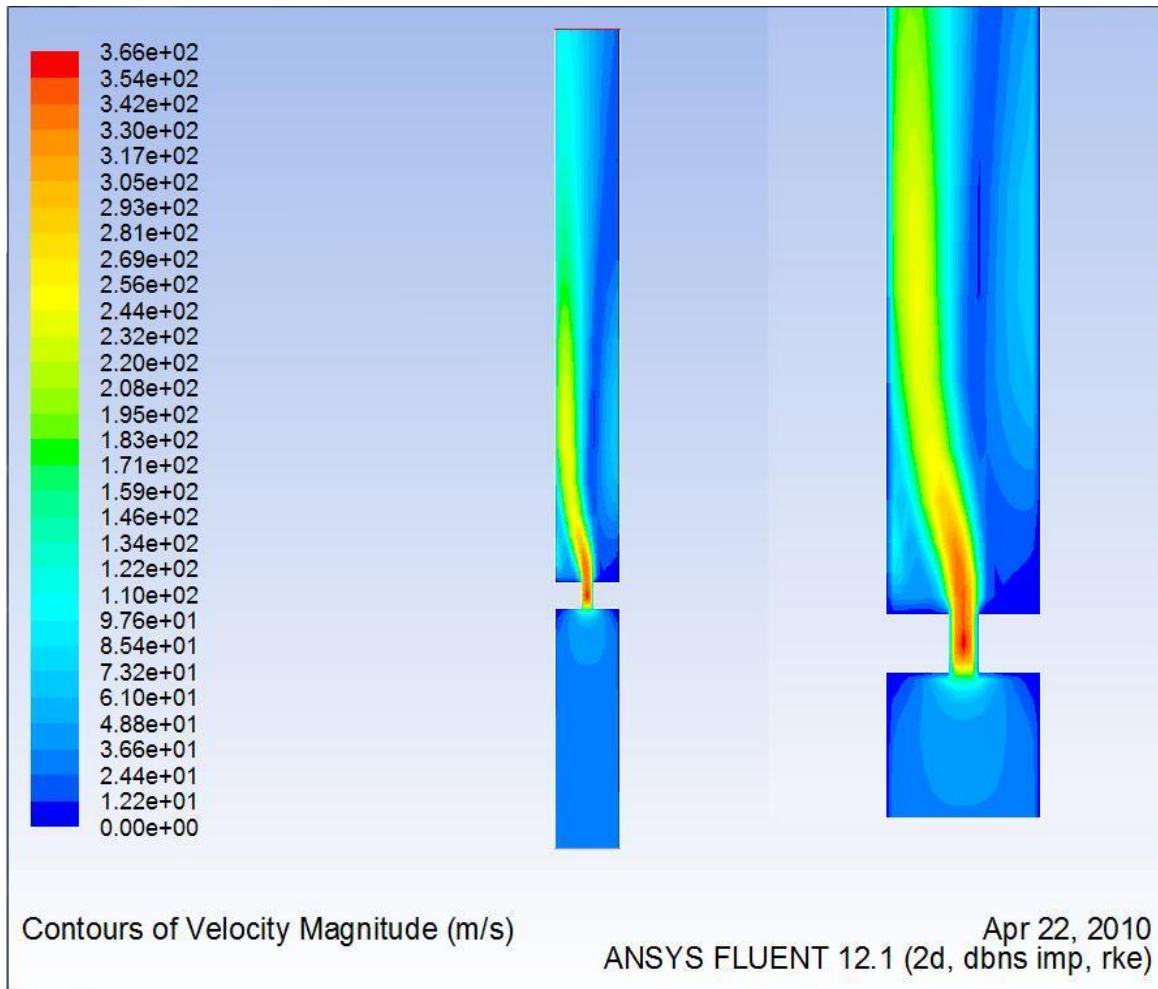


Figure 3.4: 2D planar contour velocity map 190 kPa pressure input.

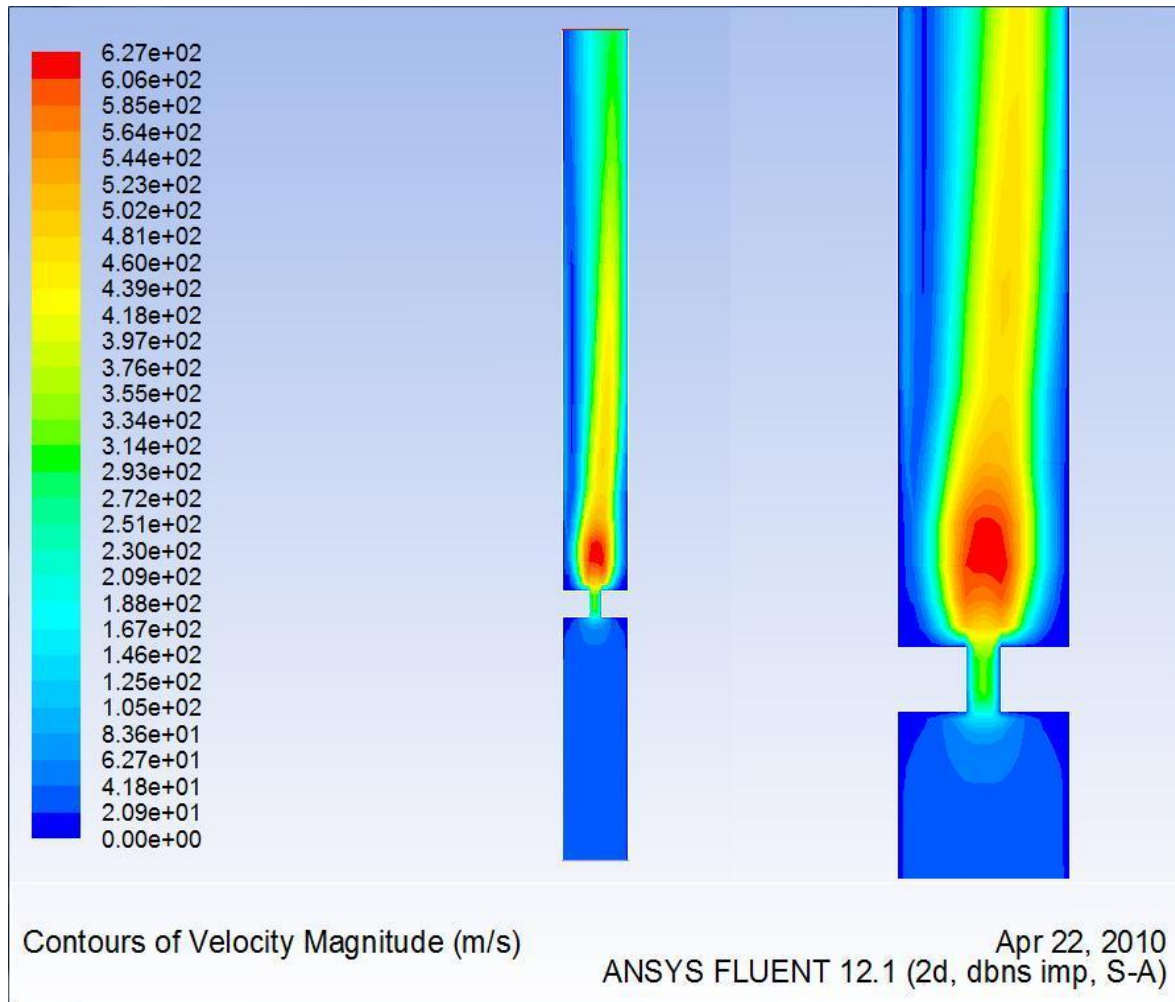


Figure 3.5: 2D planar contour velocity map 500 kPa pressure input.

Table 3.1 compares the isentropic flow velocities with the Fluent results. The isentropic single orifice model velocities are lower than those calculated by Fluent; and the comparison gives confidence that the Fluent solver settings are correct because of the reasonable agreement within 5 or 6 %.

Table 3.1: Isentropic Flow vs. 2D Planar SS Fluent Velocities

Input pressure (kPa gauge)	Isentropic Flow Velocity (m/s)	Fluent Velocity (m/s)
150	270.3	284
190	346	366
500	590	627

2D Axisymmetric Single Orifice Steady-State

The axisymmetric model was done to validate flow through a 2D orifice. This is contrasted with the 2D planar model as well as the isentropic gas dynamics solution so that we could study a simplified truncated nozzle. The planar model assumes an infinite length in the 3rd dimension whereas the axisymmetric case does not. This should limit the velocity through the orifice.

Analytical Model Formulation, 2D Axisymmetric Single Orifice

The analytical model formulation is the same as that described for the 2D SS Single Orifice.

Solver Settings

A density-based solver is used again with this model due to the high pressure-velocity coupling.

Boundary Conditions

See the 2D SS Single Orifice Boundary Conditions.

Fluent Results

There is no Coandă effect with the 2D axisymmetric model due to the restrictions of the coordinate system: the fluid can only move axisymmetrically. The speed through the orifice on this model is about 256 m/s. This is smaller than the 2D planar model, which makes sense because the flow field is now completely surrounded by a physical boundary. The 1D gas dynamics equation gives us a velocity of 267 m/s. The axisymmetric result is 4% less than the calculated 1D result, most likely because it includes viscous effects.

For the subsequent axisymmetric models, there is a notably less increase in velocity than is witnessed in the 2D planar models. This is due to restriction of the flow in the radial and axial

direction. This can be seen again in Figure 3.6 with a velocity of 323 m/s orifice velocity. At this choked pressure ratio, the velocity should be 347 m/s.

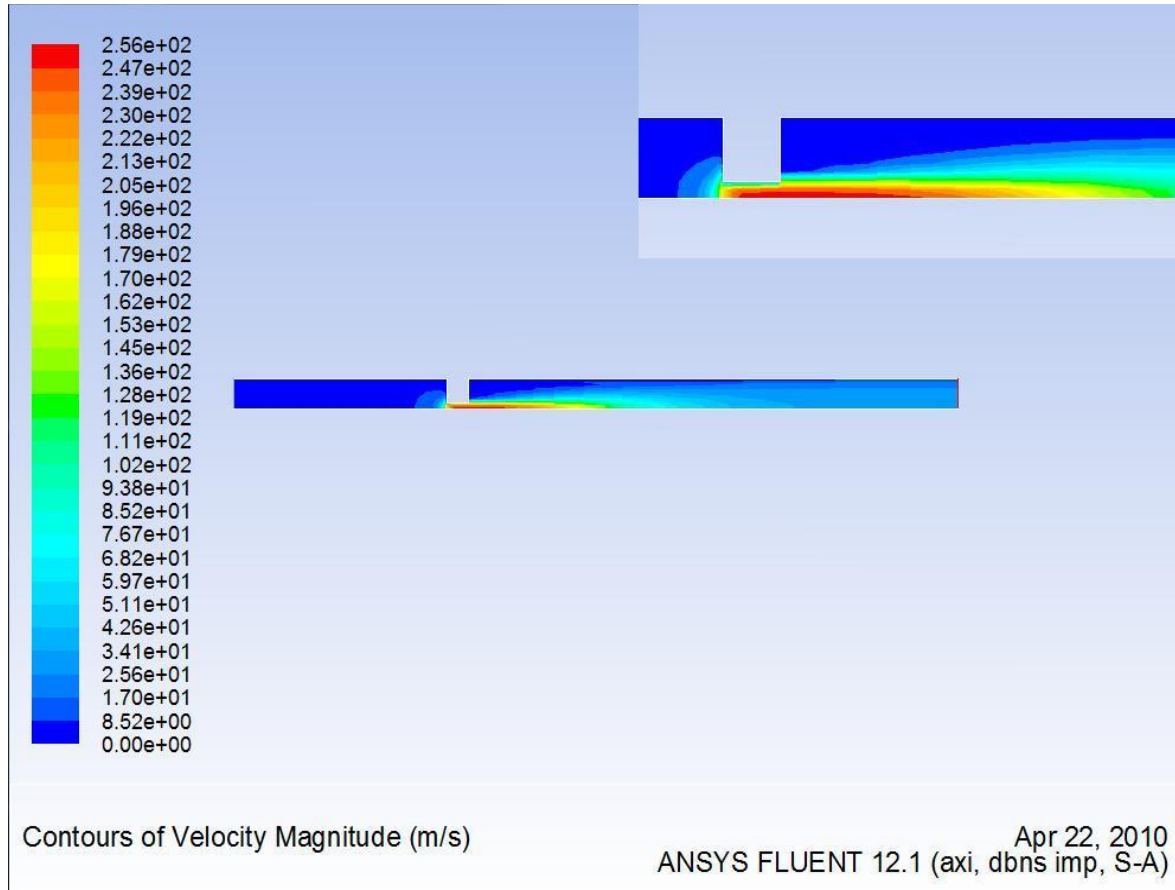


Figure 3.6: 2D axisymmetric contour velocity map 150 kPa pressure input.

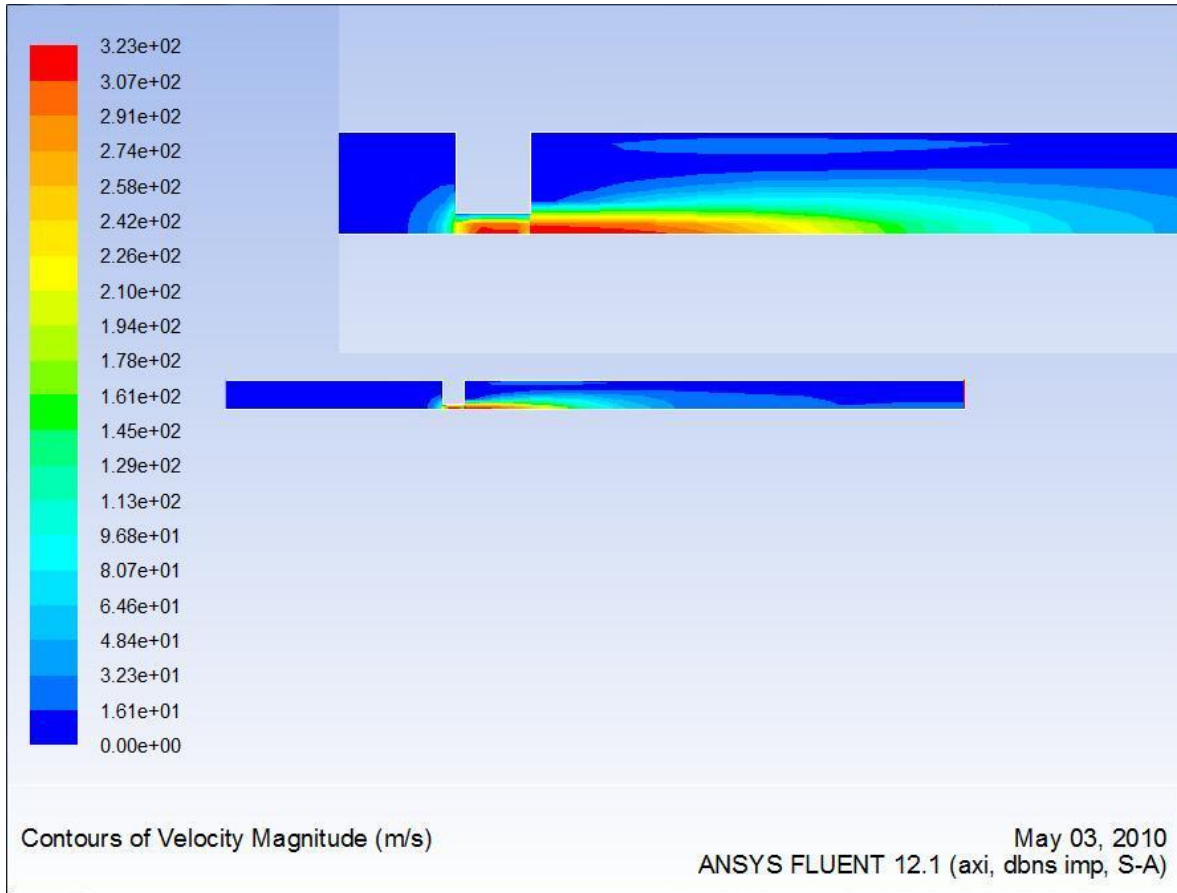


Figure 3.7: 2D axisymmetric contour velocity map 190 kPa pressure input.

Table 3.2 compares the velocities of the calculated isentropic flow values with the Fluent velocity calculations. With the axisymmetric case, all of the Fluent solutions are slower than the isentropic flow solutions and within 5 or 6% agreement.

Table 3.2: Isentropic Flow vs. 2D Axisymmetric SS Fluent Velocities

Input pressure (kPa gauge)	Isentropic Flow Velocity (m/s)	Fluent Velocity (m/s)
150	270.3	256
190	346	367

2D Single Orifice Unsteady

This is the first model that incorporated the user-defined function (UDF) with a transient pressure equation.

Analytical Model Formulation

The analytical model formulation is the same as that described in the 2D SS Single Orifice.

Determining the pressure ratio for this model will be done after the computational solution is solved. The upstream pressure is known from the derived pressure function but the stagnation pressure within the pre-chamber cannot be calculated in an unsteady case.

Solver Settings

The density-based solver was used in this model. This model was solved in the unsteady case as opposed to the steady state manner in the previous models. The rate of mass addition is calculated at the pressure inlet. Solutions at each mesh node were obtained using implicit differentiation. The energy equation was used due to compressibility effects on fluid flow.

Boundary Conditions

The initial temperature is 300 K to represent cold start conditions. The pressure user-defined function is incorporated into the pressure inlet with this model. The no slip condition is applied to the walls by selecting a velocity of zero. The inlet fluid temperature remains fixed at 300 K. All physical edges in the model will be modeled as adiabatic walls.

Initial Conditions

The initial temperature was set to 300 K (room temperature for cold start), initial velocity to 0 m/s (quiescent), and initial pressure to 0 kPa gauge.

Fluent Results

Because of the unsteady flow, the graph in Figure 3.9 was made instead of including a velocity contour map. A Coandă effect was observed as the model progressed. The maximum velocity of about 275 m/s occurred at the 280th time step (0.028 seconds). The pressure ratio (stagnation pressure divided by the pressure at the inlet) that was seen through the model was about 0.6 which would yield a velocity of 300 m/s.

Since the velocity through the orifice of the model has not reached the choked condition, the more relevant Fluent solutions will be the 150 kPa pressure input cases. It should be noted that the continuity residuals of this model were exceptionally high. More iterations per time step (300 iterations per time step were used) would most likely help to bring down the velocities.

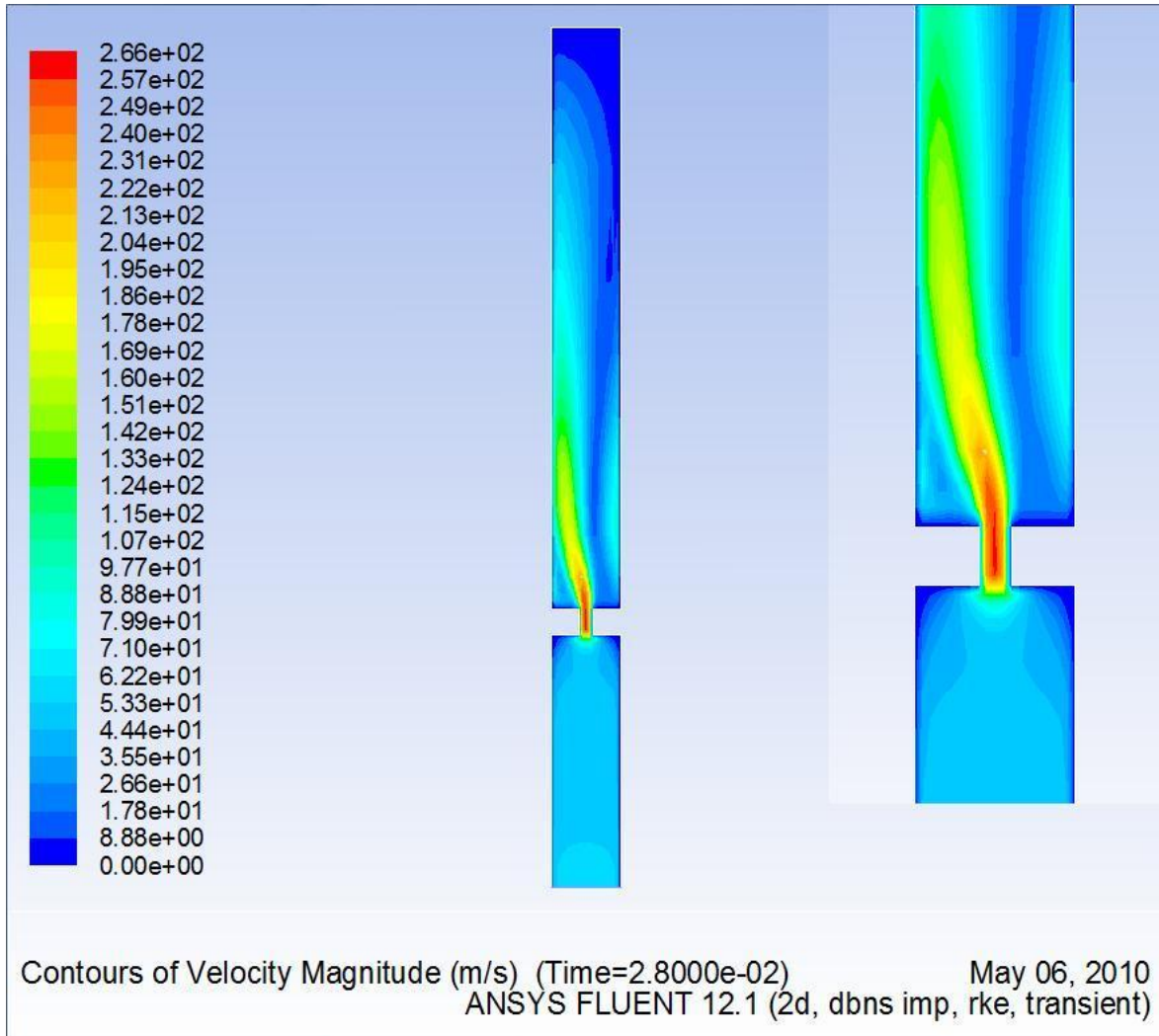


Figure 3.8: 2D planar unsteady contour velocity map at 280th time step (0.028 sec, $\theta = 151^\circ$).

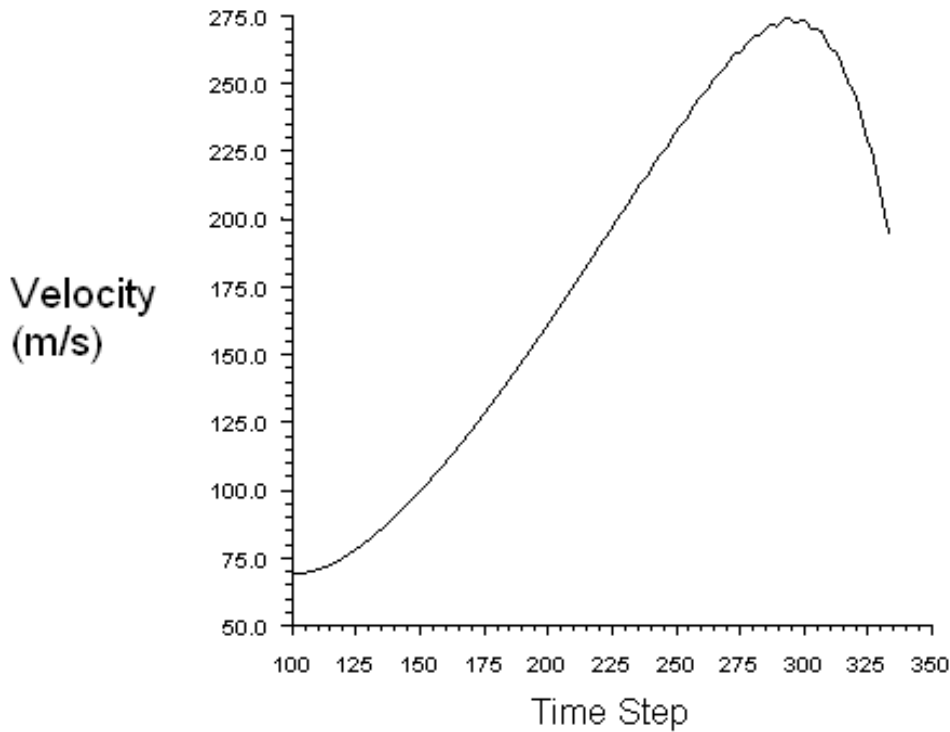


Figure 3.9: 2D unsteady model velocity profile.

3D CPT Fluid Dynamics

This model is the first to use the actual geometry of the CPT. The model includes both a study of the temperature and velocity profiles.

Analytical Model Formulation

This flow is too complicated to develop an analytical solution. It is for this reason that all of the simpler analytical flow models were developed. The CAD drawing in Figure 3.1 shows the dimensions of the CPT. A main chamber was added, as seen in the mesh of Figure 3.10, with a diameter of 1.0 inches (2.54 cm) and depth of 0.5 inches (1.27 cm) beyond the bottom of the igniter, and is concentric with the body of the CPT. An important feature of the CPT that is not easily seen in the drawings is the angular offset of the orifices. This offset creates swirling flow as fluid enters and leaves the CPT.

Boundary Conditions

The initial temperature is 300 K to represent cold start conditions. The boundary conditions with this model include the UDF from Appendix B for the pressure inlet. The no slip condition is applied to the walls by selecting a velocity of zero. All physical edges including the core will be modeled as adiabatic walls.

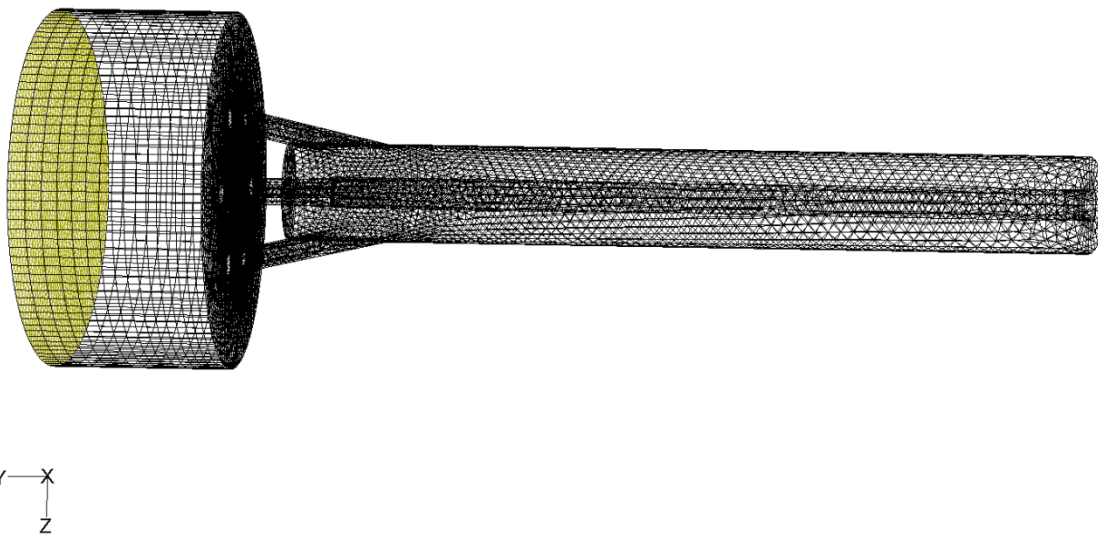


Figure 3.10: 3D CPT fluid dynamics model mesh (created in Gambit).

Initial Conditions

The initial temperature was set to 300 K (room temperature for cold start), initial velocity to 0 m/s (quiescent), and initial pressure to 0 kPa gauge.

Fluent Results

The pressure ratio observed in the Fluent results, Figure 3.11, shows that it is lowest at the 280th time step with a value of about 0.9902. This plot is important because it shows the difference between the pressures in the pre-chamber and the main chamber in the model and it is this pressure difference that drives fluid flow through the orifice. According to the isentropic flow tables, this should yield a velocity of 42 m/s. This is comparable to the maximum velocity

witnessed throughout the compression stroke in the Fluent model. As we see in Figure 3.12, the maximum velocity is about 41 m/s in the orifice.

Figure 3.13 is a slice through the middle of the CPT and displays the velocity contours when maximum velocity - about 41 m/s – occurs. The contour plot suggests that fluid tends to cling to the outside walls of the pre-chamber; whether this is due to the swirling flow induced by the orifices or a Coandă effect is uncertain. A quiescent zone is located at the bottom of the pre-chamber.

Figure 3.14, Figure 3.15, and Figure 3.16, shows the temperature rise due to compression of the flow as time progressed. This is what is expected but the temperature rise would likely be more uniform in a closed system; the inlet flow in the model here is always at 300 K. The time steps that are shown are the 50th, 280th, and 330th, which correspond to 27°, 151°, and 178° of crank shaft rotation, respectively (with 0° being BDC). A higher temperature pocket that progresses in time through the CPT is visible in each of the figures.

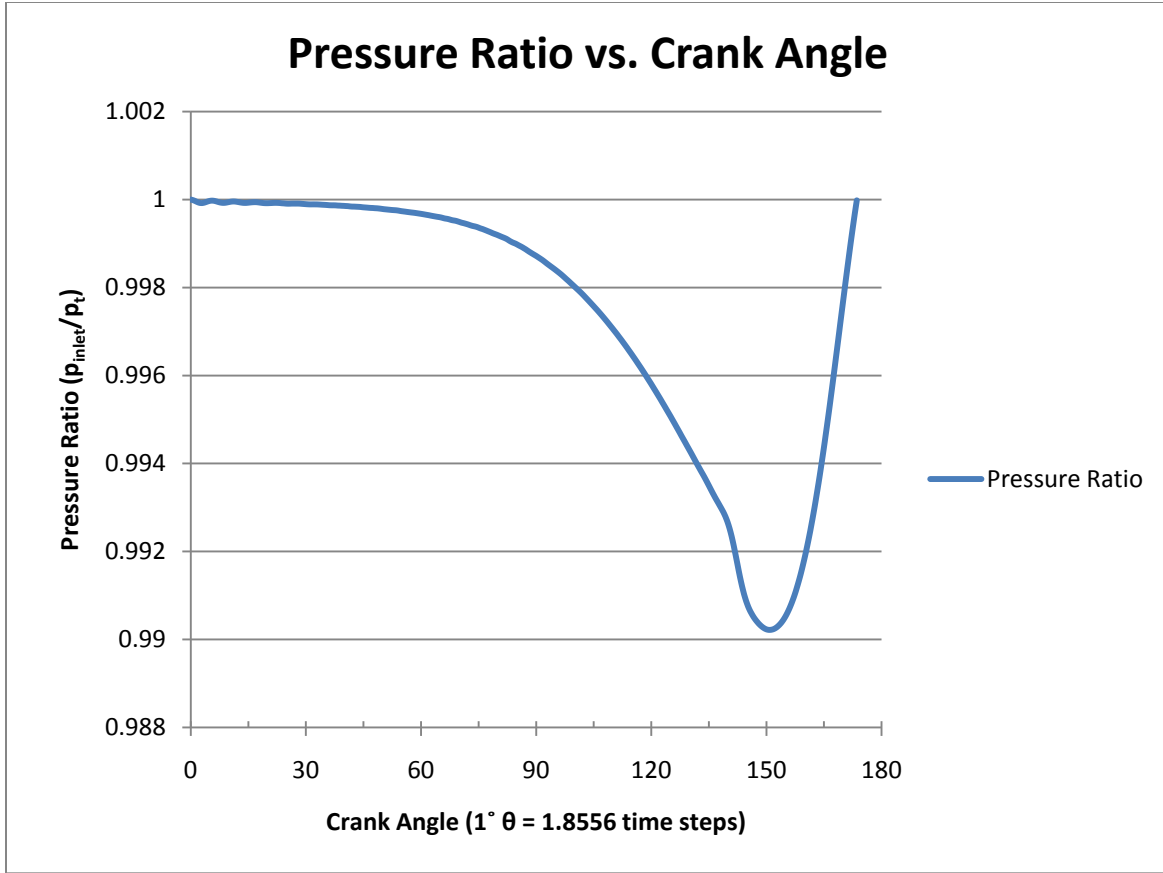


Figure 3.11: 3D CPT FM pressure ratio vs. crank angle plot.

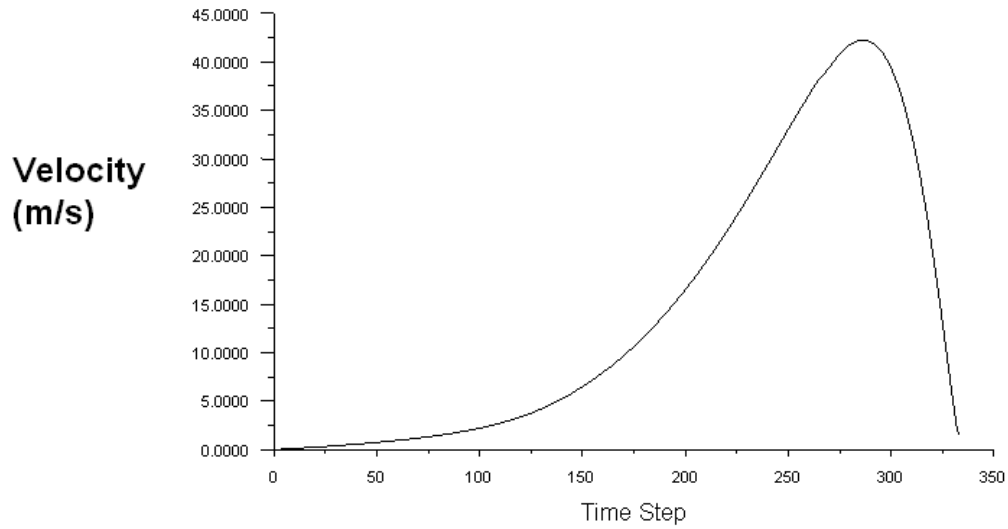


Figure 3.12: 3D CPT fluid dynamics model velocity vs. time step.

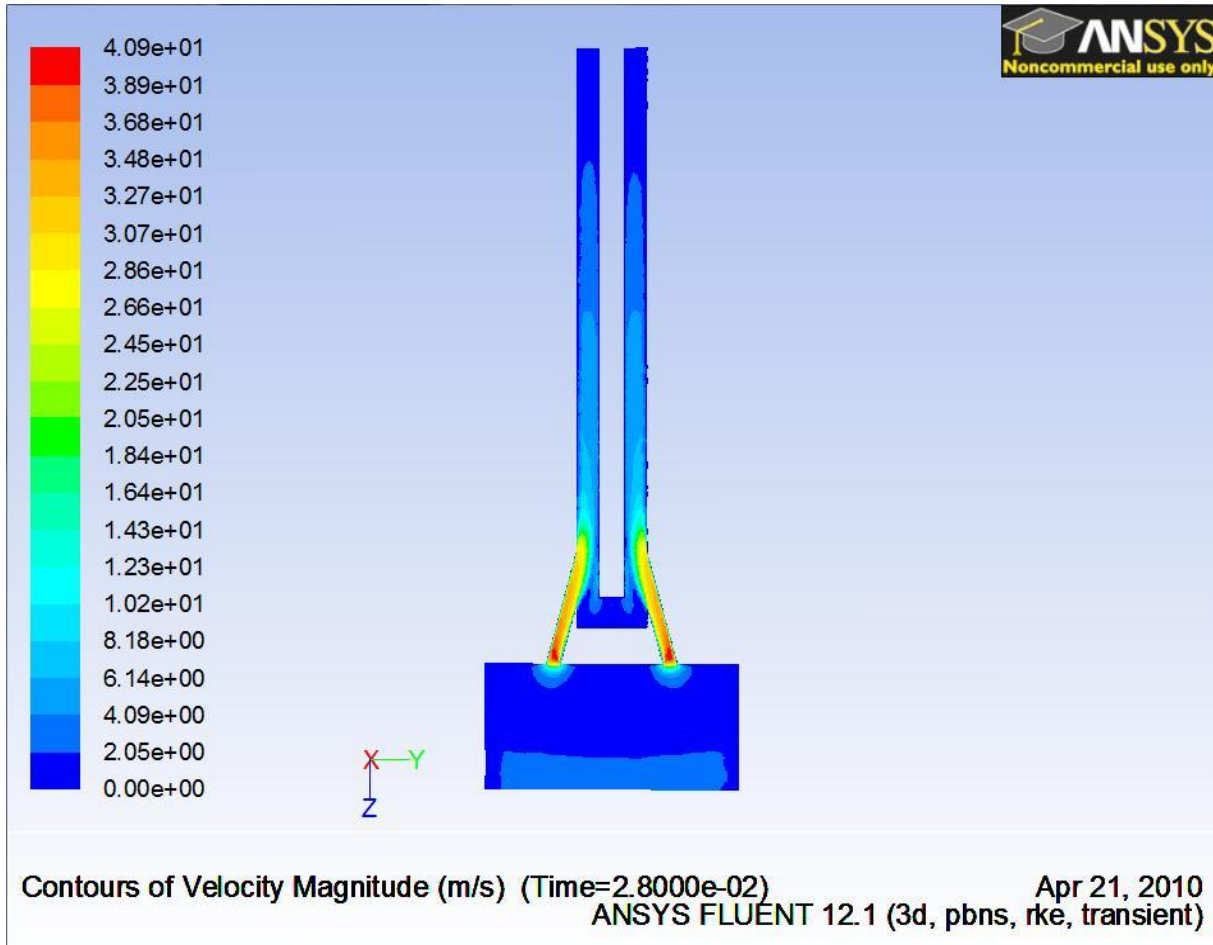


Figure 3.13: 3D CPT velocity contour map unsteady at 280th time step, 0.028 sec, $\theta = 151^\circ$.

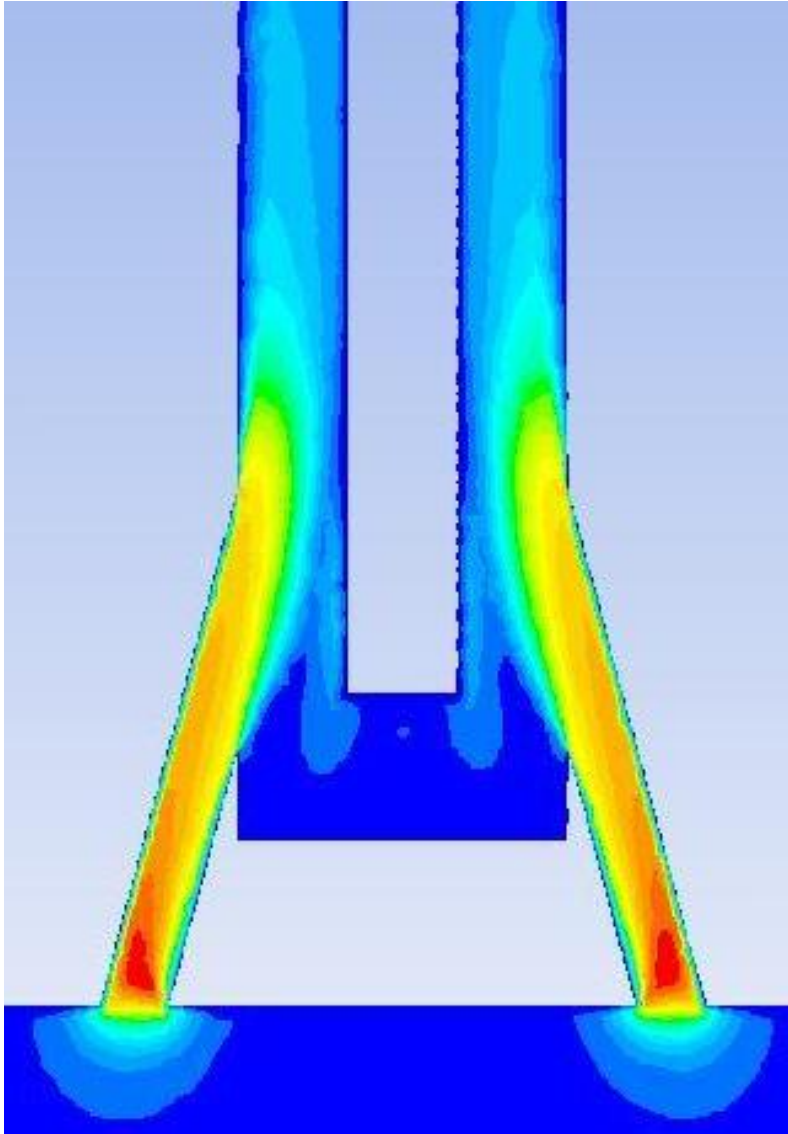


Figure 3.14: 3D CPT velocity contour map unsteady at 280th time step, magnified.

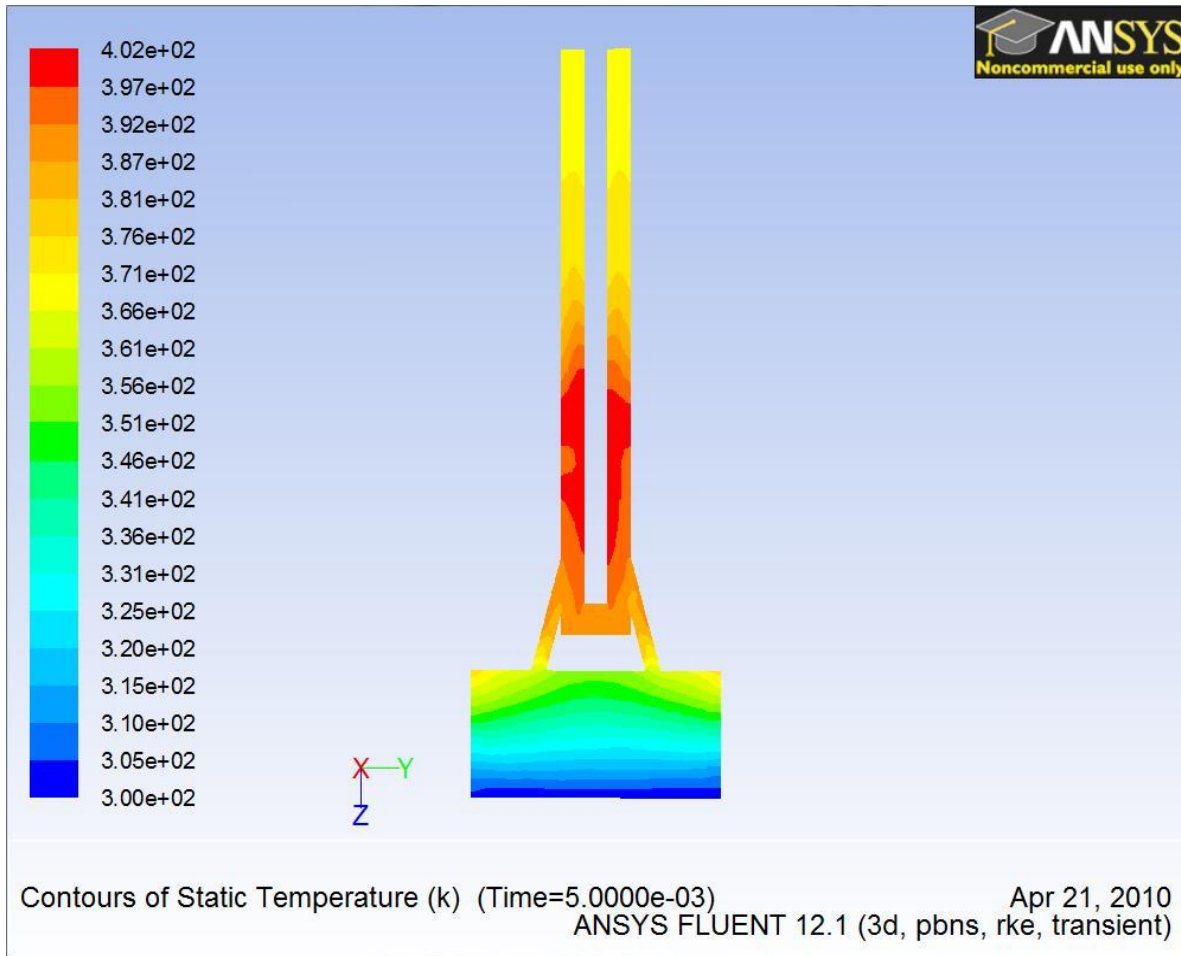


Figure 3.15: 3D CPT FM temperature contour map at $t = 0.0050$ s, $\theta = 27^\circ$.

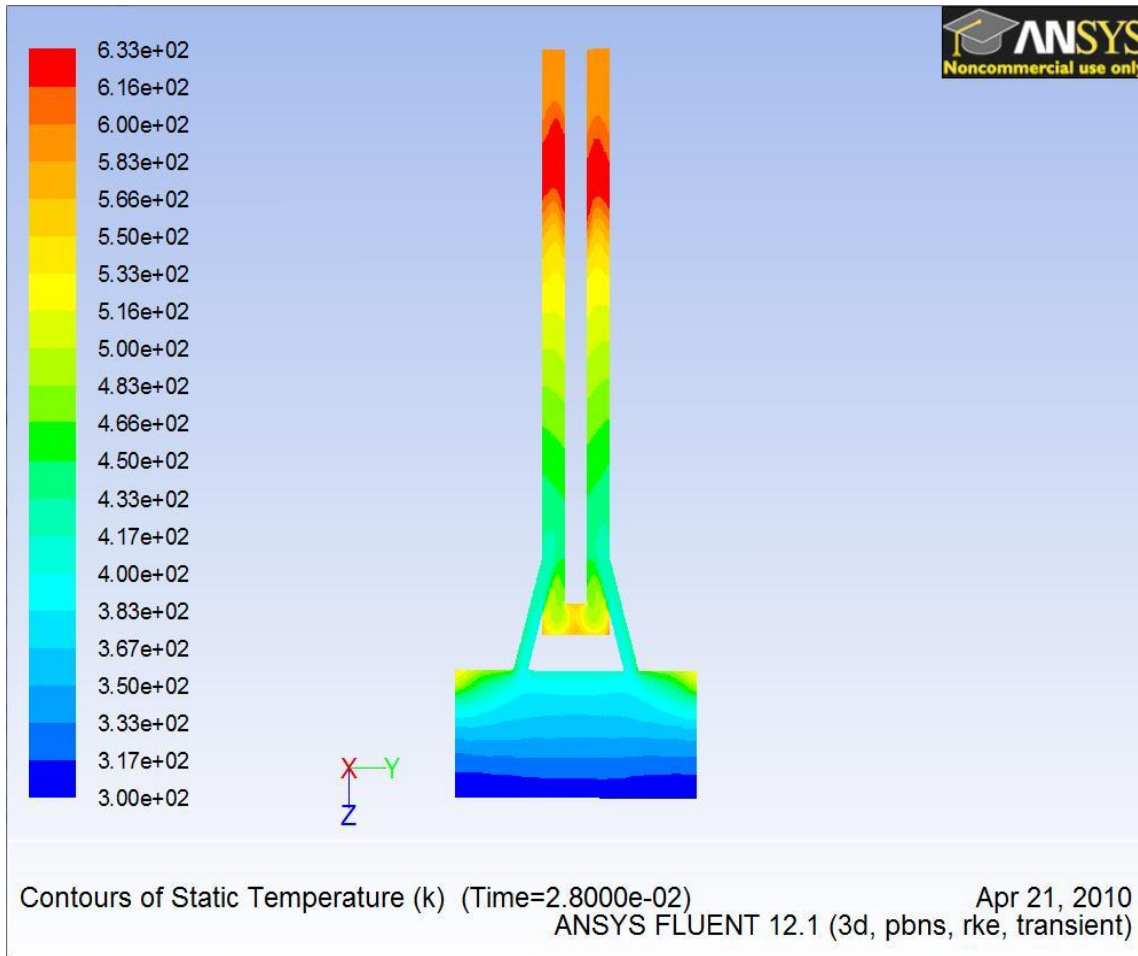


Figure 3.16: 3D CPT FM temperature contour map $t = 0.0280$ s, $\theta = 151^\circ$.

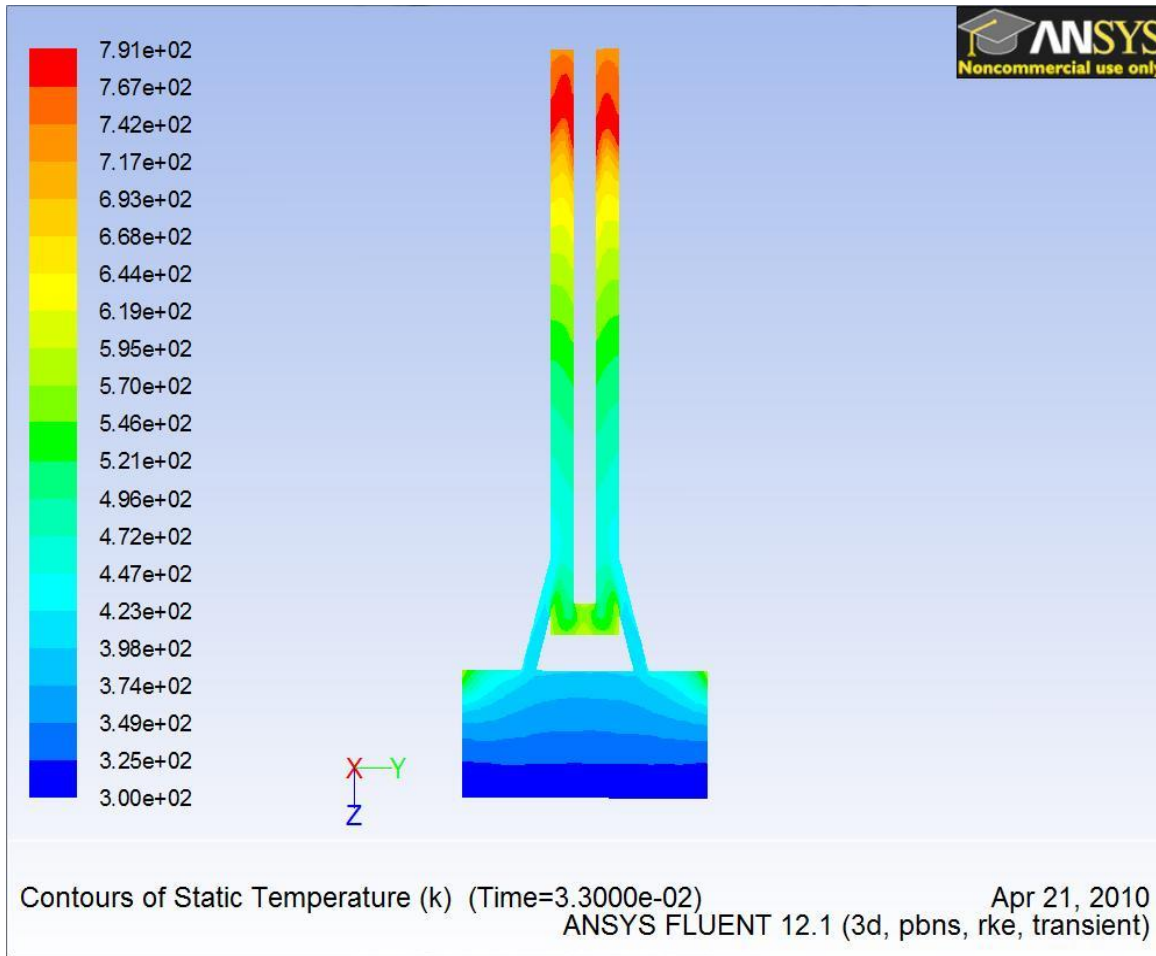


Figure 3.17: 3D CPT FM temperature contour map $t = 0.0330$ s, $\theta = 178^\circ$.

3D CPT Heat Transfer

This model includes the electrical heating of the platinum catalyst at the tip of the core. The CFD settings and boundary conditions for this model are the same as that shown for the unsteady CPT fluid model except for the heat addition. Prior steady-state heat transfer modeling including heat generation, with verification from experiments and analytical models, was done by Leichliter et al. [2008] for a coiled heated wire crosswise in plug flow. This gave us confidence in Fluent’s ability to model heat transfer phenomena including convection into a thermal boundary layer and thermal radiation effects. Figure 3.18 shows the good agreement between this Fluent model, analytical solutions, and experimental data.

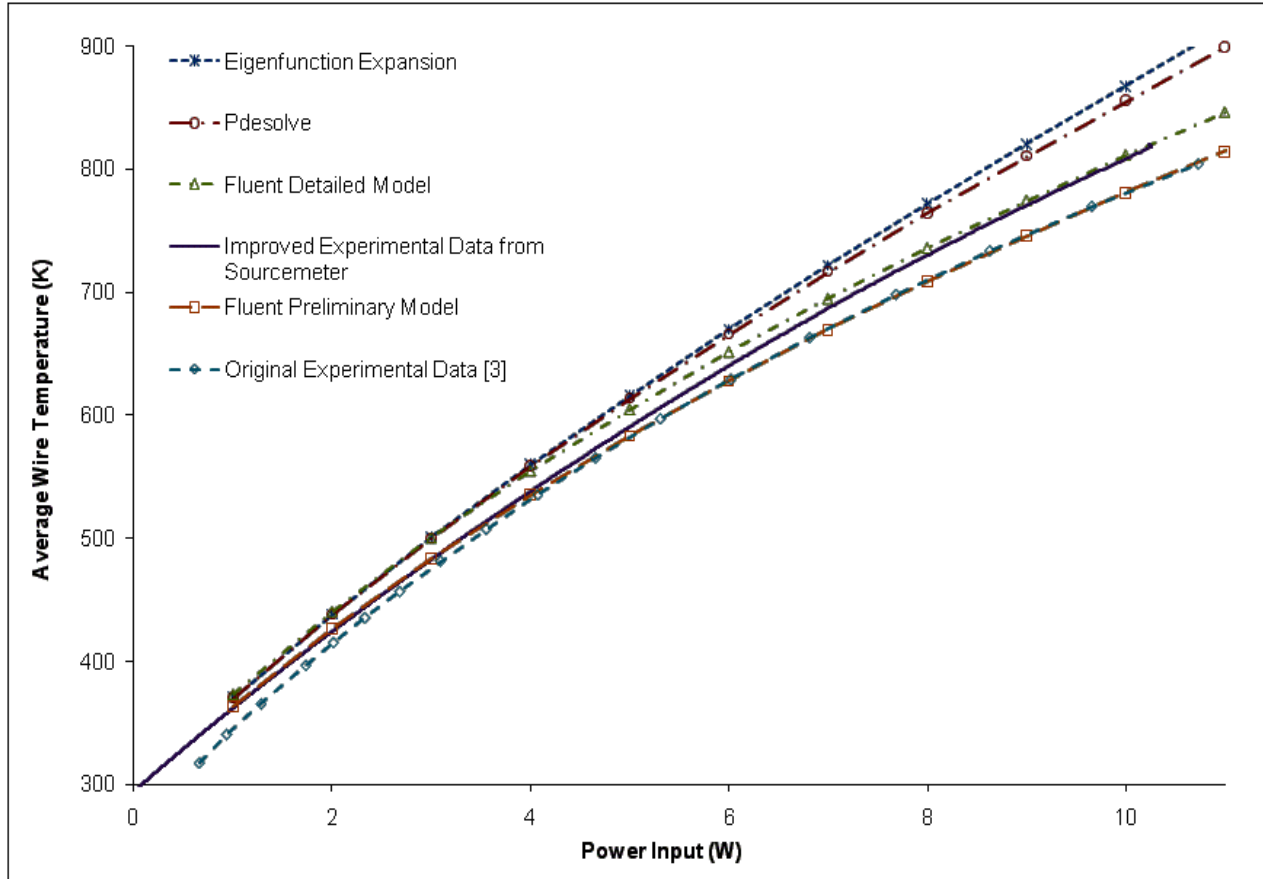


Figure 3.18: Summary of experimental data for air flow over the wire and results from the Fluent® and PDE models. [Leichliter, 2009]

Boundary Conditions

The boundary conditions for the heat transfer model are shown in Table 3.3. The initial condition and all of the boundary conditions are the same as those specified in the unsteady 3D CPT model except that the core is no longer adiabatic. Surfaces not specified as adiabatic default to a convection heat transfer boundary condition.

Table 3.3: Summary of 3D CPT Heat Transfer Model Boundary Condition Settings

Boundary Conditions	Setting	Comments	
Face	Pressure Inlet	UDF (see appendix B) T = 300 K	Calculated from volume flow rate and area of opening in quartz-tube. Temperature of inlet flow
	All remaining	Velocity at walls = 0 Adiabatic walls	No slip condition Cold start conditions

Initial Conditions

The initial temperature was set to 300 K (room temperature for cold start), initial velocity to 0 m/s (quiescent), and initial pressure to 0 kPa gauge.

Fluent Results

Figure 3.18 displays temperature contours early in the compression stroke. The core tip heating does not appear to affect the fluid mechanics of the model. The heating of the fluid in the pre-chamber due to compression has started. The fluid temperature is already hotter, due to compression, than the temperature of the core with heat generation and this situation persists for the duration of the run. At the end of the compression cycle, we produced a contour plot with a temperature range restricted between 300 K and 320 K. This allowed us to see that there was only an 8 K temperature rise within the core tip in contrast with a 400 K rise in the fluid. This may be due to low power density within the core; the electrical power was spread out over the entire volume of the core tip rather than be concentrated within the actual small volume of platinum on the surface. This detail can be addressed in future models. Nonetheless, we expect that the level of electrical heat generation used within the CPT will have minimal impact on fluid temperature. We do not expect major heat transfer impact from the catalyst until ignition occurs with the accompanying release of energy from exothermic reactions.

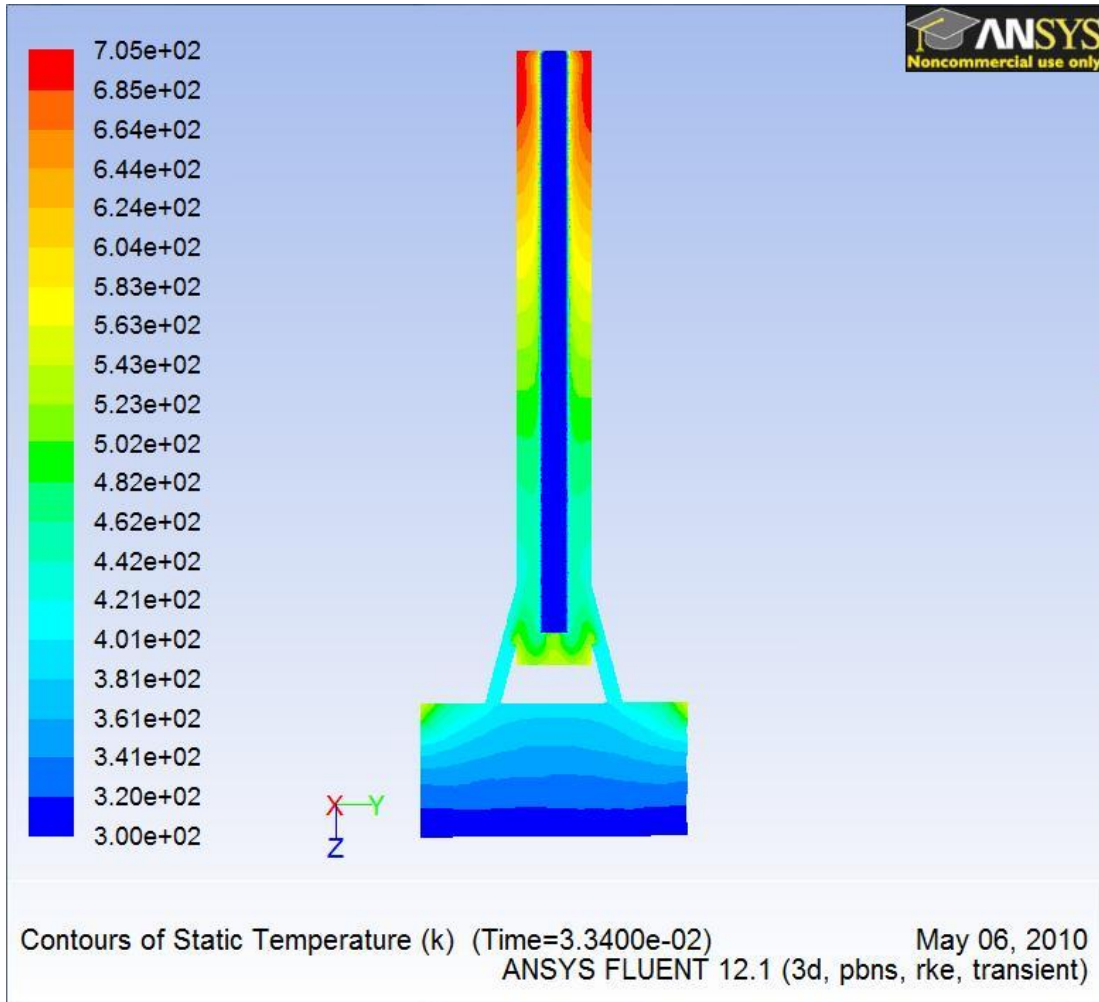


Figure 3.19: 3D CPT heat transfer temperature contour map $t = 0.0334$ s, $\theta = 180^\circ$.

3.3 Findings; Conclusions; Recommendations

After compiling the information from the preliminary models, we can conclude that the calibration of the Fluent settings for the 3D real geometrical model are correct. The solutions of the steady state problems indicate that there is no need to take supersonic speed into account with the inclusion of more orifices. The single orifice models gave us a means to check CFD flow through an orifice.

Table 3.4 shows a summary between the isentropic flow calculated velocities and that of the Fluent solutions. There is good agreement - within 5 and 6% - between the gas dynamics equation solution and all of the numerical solutions from Fluent. We observed a Coandă effect in the 2D Planar model. These results suggest the process of developing a series of simpler models is useful in gaining confidence in the CFD program.

The maximum cell skewness in the meshing did not exceed 0.84. This indicates that the mesh density was sufficient to maintain the solution continuity within the grid. Hence the code could accurately model large changes in velocity and temperature within the complex geometry.

Table 3.4: Summary of Steady State Single Orifice Models

	Isentropic Flow	2D Planar	2D Axisymmetric
Input pressure (kPa gauge)	(m/s)	(m/s)	(m/s)
150	270	284	256
190	346	367	323

CFD and Heat Transfer of CPT

The unsteady CPT model was run with a pressure-based solver. The velocity of this model is in good agreement with the isentropic flow tables; we observe a maximum of about 42 m/s which agrees with an isentropic flow velocity of 41 m/s.

From examining the flow pattern, it appears that the flow through the orifices is bypassing the quiescent zone and part of the heated core.

The thermal penetration depth in brass for the three hundredths of a second span of the model was calculated to be 0.005 mm. This value is small relative to the geometry of the igniter; the adiabatic wall assumption is appropriate.

Results of Heat Transfer Modeling

The heat transfer modeling in the unsteady models with and without the heated catalyst shows formation of high temperature pockets both towards the top of the igniter and in the quiescent zone off of the tip. These high temperature pockets are most likely due to fluid compression. But compression heating should happen uniformly throughout the control volume of the pre-chamber and main chamber. The reason why it does not is because this first CPT is being modeled as an open system and at the pressure inlet, we assume a constant 300 K temperature for all mass entering.

A compression ratio of 9 to 1 was selected. The data from Figure 3.20 (volume-average density of the control volume) shows that the ratio of the beginning and final densities are actually 16.6 to 1. This demonstrates that mass is added to the system.

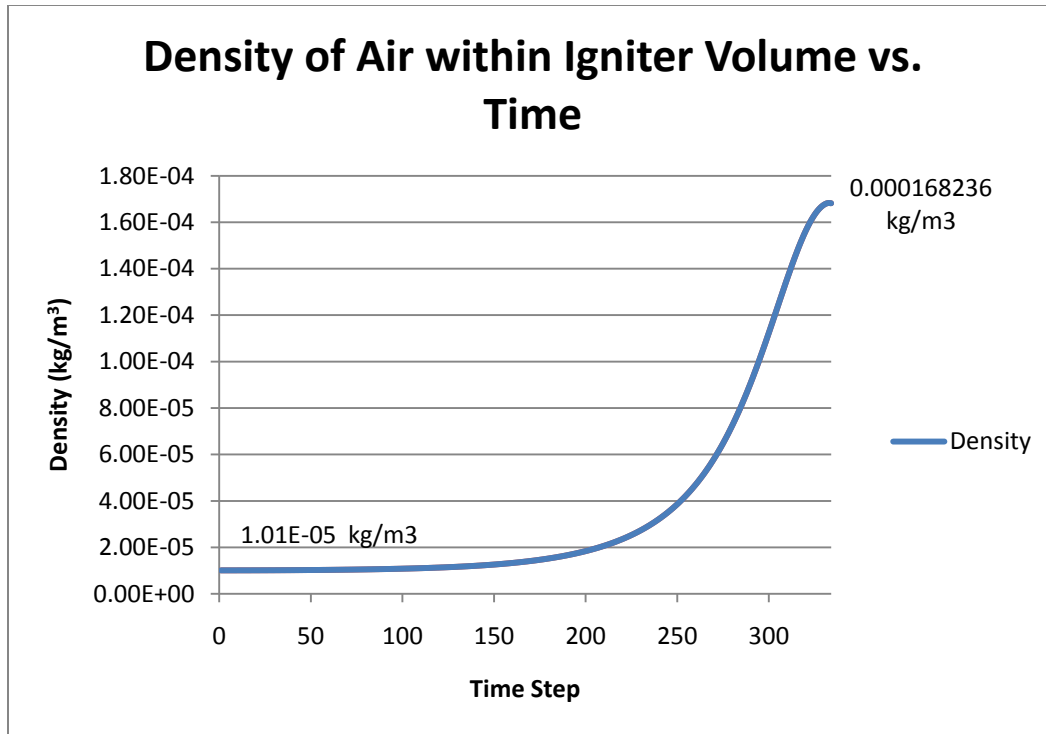


Figure 3.20: Density plot of the control volume of the igniter.

Fluent calculated a volume-averaged temperature of 413 K at the final time step. The volume-averaged temperature can be compared with that calculated from the ideal gas law:

$$T_2 = T_1 \frac{\rho_1 P_2}{\rho_2 P_1} = 300K \frac{1}{16.6} 21.6 = 392K$$

The contours in Figure 3.19 show a maximum temperature of 791 K. At present we have no method of verifying the validity and magnitude of the different hot spots within the complex fluid mechanics; it appears that a thermal wave is passing through the compressing gases. Whether this phenomenon is real or a computation anomaly remains to be discovered.

The current heat transfer model does show that the heating occurring at the core tip is negligible compared to the heating of the fluid around it. This is due to compression, the power density, and how the igniter was modeled.

Future Work

It would be beneficial to further validate the turbulence model of the CPT by checking the mesh independence of the solution and/or by flow visualization – the latter being the more difficult challenge.

A future version of the CPT model will incorporate a moving boundary along the face where the pressure inlet is currently located. This will model the gas compression (and heating) of a piston moving towards top dead center in a closed-mass system. Appropriate fast-solving sub-problems should be developed first to understand how to use and verify the moving boundary in the CPT model.

Heat generation can be refined by using the actual volume of platinum wire coiled around the tip and the appropriate electrical power density. Future models may consider pre-heated platinum by specifying a higher initial temperature.

Before including chemical kinetics, there needs to be some research done with the thermal boundary layers on the surface of the platinum catalyst. The mesh sizing will likely need to be altered in this region because of the expected high temperature gradients.

Before adding surface and gas phase combustion kinetics to the CPT model, the Fluent-Chemkin interaction should be applied to a simpler model such as a model of a heated Pt wire in cross flow where additional experimental data may be obtained for model validation.

REFERENCES

- [1] Cherry, M. A., and Elmore, C. L., 1990, "Timing Chamber Ignition Method and Apparatus," *US Patent*, 4,997,873.
- [2] Cherry, M. A., Morrisset, R., and Beck, N., 1992, "Extending the Lean Limit with Mass-Timed Compression Ignition using a Plasma Torch," *Society of Automotive Engineers Paper*, 921556.
- [3] Cherry, M. A., 1992, "Catalytic-Compression Timed Ignition," *US Patent*, 5,109,817.
- [4] Leichliter, K., Lounsbury, B., Steciak, J., Budwig, R., and Beyerlein, S., 2008, "Finite Element Model of a Heated wire Catalyst in Cross Flow," *ASME Paper IMECE2008-68922*.
- [5] Leichliter, K. J., Steciak, J., Budwig, R., Beyerlein, S., 2010, "Measuring Ignition Temperature and Heat Generation from Moist Propane-Oxygen Mixtures on Platinum," *ASME Paper IMECE2010-38861*.
- [6] Cordon, D., Beyerlein, S., Steciak, J., and Cherry, M., 2008, "Homogeneous Charge Catalytic Ignition of Ethanol-Water/Air Mixtures in a Reciprocating Engine," *ASME Paper IMECE2008-68999*.
- [7] Cordon, D., Beyerlein, S., Steciak, J., and Cherry, M., 2008, "Conversion of a Homogeneous Charge Air-Cooled Engine for Operation on Heavy Fuels," *Society of Automotive Engineers Paper 2008-32-0023*.
- [8] Cordon, D., Walker, M., Beyerlein, S., Steciak, J., and Cherry, M., 2006, "Catalytically Assisted Combustion of JP-8 in a 1 kW Low-Compression Genset," *Society of Automotive Engineers Paper 2006-32-0024*.
- [9] Olberding, J., Cordon, D., Beyerlein, S., Steciak, J., and Cherry, M., 2005, "Dynamometer Testing of an Ethanol-Water Fueled Transit Van," *SAE Transactions, Journal of Fuels and Lubricants*, **114-5**, (2005-01-3706), pp. 1253 – 1264.
- [10] Cordon, D., Clarke, E., Beyerlein, S., Steciak, J. and Cherry, M., 2002, "Catalytic Igniter to Support Combustion of Ethanol-Water/Air Mixtures in Internal Combustion Engines," *Society of Automotive Engineers Paper 2002-01-2863*.
- [11] Morton, A., Munoz-Torrez, G., Beyerlein, S., Steciak, J., McIlroy, D., and Cherry, M., 1999, "Aqueous Ethanol Fueled Catalytic Ignition Engine," *Society of Automotive Engineers Paper 1999-01-3267*.
- [12] Hanlon, M.A., Ma, H.B., 2003, "Evaporation heat transfer in sintered porous media," *Journal of Heat Transfer*, **125** (4), pp. 644-652.
- [13] Pei-Xue, J., Rui-Na, X., Meng, L., 2004, "Experimental investigation of convection heat transfer in mini-fin structures and sintered porous media," *Journal of Enhanced Heat Transfer*, **11** (4), pp. 391-405.

- [14] Wei, L., Ting-Zhen, M., 2008, "Analysis for heat transfer enhancement in the flow of a tube filled with porous media at different layers," *Zhongguo Dianji Gongcheng Xuebao/Proceedings of the Chinese Society of Electrical Engineering*, v 28, n 32, p 66-71.
- [15] Hetstroni, G., Gurevich, M., Rozenblit, R., 2006, "Sintered porous medium heat sink for cooling of high-power mini-devices, International," *Journal of Heat and Fluid Flow*, **27** (2), pp. 259-266.
- [16] Singh, R., Akbarzadeh, A., Mochizuki, M., 2009, "Sintered porous heat sink for cooling of high-powered microprocessors for server applications," *International Journal of Heat and Mass Transfer*, **52** (9-10), pp. 2289-2299.
- [17] McCormick, R. and Parish, R., 2001, *Advanced Petroleum Based Fuels Program and Renewable Diesel Program*, National Renewable Energy Laboratory, NREL/MP-540-32674.
- [18] Park, S., Yoon, S., Suh, and H., Lee, C., 2008, "Effect of the Temperature Variation on Properties of Biodiesel and Biodiesel-Ethanol blends fuels," *Oil and Gas Science and Technology*, **63** (6) pp. 737-745.
- [19] Stone, R., 1999, *Introduction to Internal Combustion Engines*, SAE International, Warrendale, PA, USA.
- [20] Holman, J. P., 1971, *Experimental Methods for Engineers*, 2nd ed., McGraw-Hill, New York, pp. 244-246, Chap. 8.
- [21] *Handbook of Chemistry and Physics*, 61st Edition, CRC Press, Boca Raton, FL, USA, p. F-173.
- [22] Darling A. S., 1966, "The Elastic and Plastic Properties of the Platinum Metals," *Platinum Metal Rev.*, **10** (1), pp. 14-19.
- [23] Tsutsumi Kazuhiko, Yamashita Akira, and Ohji Hiroshi, 2002, "The Experimental Study of High TCR Pt Thin Films for Thermal Sensors," *Proceedings of IEEE Sensors*, **1** (2), pp. 1002-1005.
- [24] Perger, T., Kovács, T., Turányi, T., and Treviño, C., "Determination of Adsorption and Desorption Parameters from Ignition Temperature Measurements in Catalytic Combustion Systems," *Journal of Physical Chemistry B*, B107(10):2262-2274, 2003.
- [25] Perger, T., Kovács, T., Turányi, T., and Treviño, C., "Determination of the adsorption and desorption parameters for ethane and propene from measurements of the heterogeneous ignition temperature," *Combustion and Flame*, 142:107-116, 2005.